Linköping Studies in Science and Technology. Dissertation No 1226.

Growth and characterisation of InGaAs-based quantum dots-in-a-well infrared photodetectors

Linda Höglund

Linköping 2008

ISSN : 0345-7524
ISBN : 978-91-7393-741-2

Cover design by Ingrid Bergman

Printed by LiU-Tryck, Linköping University, Sweden

Abstract

This thesis presents results from the development of quantum dot (QD) based infrared photodetectors (IPs). The studies include epitaxial growth of QDs, investigations of the structural, optical and electronic properties of QD-based material as well as characterisation of the resulting components.

Metal-organic vapour phase epitaxy is used for growth of self-assembled indium arsenide (InAs) QDs on gallium arsenide (GaAs) substrates. Through characterisation by atomic force microscopy, the correlation between size distribution and density of quantum dots and different growth parameters, such as temperature, InAs deposition time and V/III-ratio (ratio between group V and group III species) is achieved. The V/III-ratio is identified as the most important parameter in finding the right growth conditions for QDs. A route towards optimisation of the dot size distribution through successive variations of the growth parameters is presented.

The QD layers are inserted in $In_{0.15}Ga_{0.85}As/GaAs$ quantum wells (QWs), forming so-called dots-in-a-well (DWELL) structures. These structures are used to fabricate IPs, primarily for detection in the long wavelength infrared region (LWIR, 8-14 μm).

The electron energy level schemes of the DWELL structures are revealed by a combination of different experimental techniques. From Fourier transform photoluminescence (FTPL) and FTPL excitation (FTPLE) measurements the energy level schemes of the DWELL structures are deduced. Additional information on the energy level schemes is obtained from tunneling capacitance measurements and the polarization dependence studies of the interband transitions. From tunneling capacitance measurements, the QD electron energy level separation is confirmed to be 40-50 meV and from the polarization dependence measurements, the heavy hole character of the upper hole states are revealed.

Further characterisation of the IPs, by interband and intersubband pho-

tocurrent measurements as well as dark current measurements, is performed. By comparing the deduced energy level scheme of the DWELL structure and the results of the intersubband photocurrent measurements, the origin of the photocurrent is determined. The main intersubband transition contributing to the photocurrent is identified as the QD ground state to a QW excited state transition. Optical pumping is employed to gain information on the origin of an additional photocurrent peak observed only at temperatures below 60 K. By pumping resonantly with transitions associated with certain quantum dot energy levels, this photocurrent peak is identified as an intersubband transition emanating from the quantum dot excited state. Furthermore, the detector response is increased by a factor of 10, when using simultaneous optical pumping into the quantum dots states, due to the increasing electron population created by the pumping. In this way, the potentially achievable responsivity of the detector is predicted to be 250 mA/W.

Significant variations of photocurrent and dark currents are observed, when bias and temperature are used as variable parameters. The strong bias and temperature dependence of the photocurrent is attributed to the escape route from the final state in the QW, which is limited by tunneling through the triangular barrier. Also the significant bias and temperature dependence of the dark current could be explained in terms of the strong variation of the escape probability from different energy states in the DWELL structure, as revealed by interband photocurrent measurements. These results are important for the future optimisation of the DWELL IP.

Tuning of the detection wavelength within the LWIR region is achieved by means of a varying bias across the DWELL structure. By positioning the InAs quantum dot layer asymmetrically in a 8 nm wide $In_{0.15}Ga_{0.85}As/GaAs$ quantum well, a step-wise shift in the detection wavelength from 8.4 to 10.3 μm could be achieved by varying the magnitude and polarity of the applied bias. These tuning properties could be essential for applications such as modulators and dual-colour infrared detection.

Preface

The work presented in this thesis has been performed within the frame of an industrial PhD project at the Nanoelectronics department at Acreo, Sweden and at Linköping University, Sweden in the Material Science Division at the Department of Physics, Chemistry and Biology (IFM). Some experiments have been performed at the Solid State Physics Department at Lund University and at the Center for Applied Mathematics and Physics at Halmstad University, Sweden.

The thesis is divided into two parts. The first part gives a general introduction to the physics of semiconductors, the growth of semiconductors and to the application of interest in this work - infrared detectors. The second part contains a collection of the following papers:

Papers included in the thesis

I. Optimising uniformity of InAs/(InGaAs)/GaAs quantum dots grown by metal organic vapor phase epitaxy
L. Höglund, E. Petrini, C. Asplund, H. Malm, P. O. Holtz, J. Y. Andersson, Applied Surface Science 252 (2006) 5525.
(My contribution: Growth, optical measurements, analysis, writing)

II. Origin of photocurrent in lateral quantum dots-in-a-well infrared photodetectors
L. Höglund, P.O. Holtz, C. Asplund, Q. Wang, S. Almqvist, H. Malm, E. Petrini, H. Pettersson, J. Y. Andersson, Applied Physics Letters 88 (2006) 213510.
(My contribution: Measurements, analysis, writing)

III. Bias and temperature dependence of the escape processes in quantum dots-in-a-well infrared photodetectors
L. Höglund, P. O. Holtz, H. Pettersson, C. Asplund, Q. Wang, S. Almqvist, S. Smuk, E. Petrini, J. Y. Andersson, Applied Physics Letters 93 (2008) 103501.
(My contribution: Photocurrent measurements, analysis, writing)

IV. Bias mediated tuning of the detection wavelength in asymmetrical quantum dots-in-a-well infrared photodetectors
L. Höglund, P. O. Holtz, H. Pettersson, C. Asplund, Q. Wang, S. Almqvist, H. Malm, E. Petrini, J. Y. Andersson, Accepted for publication in Applied Physics Letters, 2008.
(My contribution: Measurements, analysis, writing)

V. Optical pumping as artificial doping in quantum dots-in-a-well infrared photodetectors
L. Höglund, P. O. Holtz, H. Pettersson, C. Asplund, Q. Wang, S. Almqvist, H. Malm, E. Petrini, J. Y. Andersson, Accepted for publication in Applied Physics Letters, 2008.
(My contribution: Measurements, analysis, writing)

VI. Energy level scheme of an InAs/InGaAs/GaAs quantum dots-in-a-well infrared photodetector structure
L. Höglund, K. F. Karlsson, P. O. Holtz, H. Pettersson, C. Asplund, Q. Wang, S. Almqvist, H. Malm, E. Petrini, J. Y. Andersson, Manuscript.
(My contribution: Parts of measurements, analysis, writing)

Papers not included in the thesis

i. A cross-sectional scanning tunneling microscopy study of a quantum dot infrared photodetector structure
L. Ouattara, A. Mikkelsen, E. Lundgren, L. Höglund, C. Asplund, J. Y. Andersson, Journal of Applied Physics, 100 (2006) 44320.

ii. Quantum dots-in-a-well infrared photodetectors for long wavelength infrared detection
L. Höglund, P. O. Holtz, L. Ouattara, C. Asplund, Q. Wang, S. Almqvist, E. Petrini, H. Malm, J. Borglind, A. Mikkelsen, E. Lundgren, H. Pettersson, J. Y. Andersson, Proceedings of SPIE 6401 (2006) 640109-1.

iii. Multilayer InAs/InGaAs quantum dot structure grown by MOVPE for optoelectronic device applications
Q. Wang, L. Höglund, S. Almqvist, B. Noharet, C. Asplund, H. Malm, E. Petrini, M. Hammar, J. Y. Andersson, Proceedings of SPIE 6327 (2006) 63270L-1.

iv. Tuning of the detection wavelength in quantum dots-in-a-well infrared photodetectors
L. Höglund, P. O. Holtz, C. Asplund, Q. Wang, S. Almqvist, E. Petrini, H. Malm, H. Pettersson, J. Y. Andersson, Proceedings of SPIE 6940 (2008) 694002-1.

v. Optical reflection from excitonic quantum-dot multilayer structures
Y. Fu, H. Ågren, L. Höglund, J. Y. Andersson, C. Asplund, M. Qiu, L. Thylén, Appl. Phys. Lett. 93 (2008) 183117.

Conference presentations

InAs/InGaAs quantum dots grown by MOVPE
Linda Höglund, E. Petrini, C. Asplund, H. Malm, B. Noharet, J. Y. Andersson Optik i Sverige 2004, November 9 2004, Linköping, Sweden, Poster.

The influence of different growth parameters on the uniformity of InAs/(InGaAs)/GaAs quantum dots grown by metal organic vapor phase epitaxy
L. Höglund, E. Petrini, C. Asplund, H. Malm, P. O. Holtz, J. Y. Andersson Acsin-8/ICTF-13 2005, June 19-23 2005, Stockholm, Sweden, Paper I, Poster.

Quantum dots-in-a-well infrared photodetectors for long wavelength infrared photodetectors
L. Höglund, C. Asplund, Q. Wang, S.Almqvist, J. Borglind, P. O. Holtz, J. Y. Andersson, Northern Optics 2006, June 14-16 2006, Bergen, Norway, Poster.

On the Origin of the Photoconductivity in Lateral Quantum Dots-in-a-Well Infrared Photodetectors
L. Höglund, P. O. Holtz, C. Asplund, Q. Wang, S. Almqvist, H. Malm, E. Petrini, H. Pettersson, J. Y. Andersson International Conference on the Physics of Semiconductors (ICPS)- 28, July 24-28 2006, Vienna, Austria, Poster.

Quantum dots-in-a-well infrared photodetectors for long wavelength infrared photodetectors
L. Höglund, P. O. Holtz, L. Ouattara, C. Asplund, Q. Wang, S. Almqvist, E. Petrini, H. Malm, J. Borglind, A. Mikkelsen, E. Lundgren, H. Pettersson, J. Y. Andersson, SPIE Europe, Optics and Photonics in Security and Defence, September 11-14 2006, Stockholm, Sweden, Invited talk, paper ii.

Performance of Quantum Dots-in-a-Well Infrared Photodetectors - Status and Prospects
L. Höglund, P. O. Holtz, C. Asplund, Q. Wang, S. Almqvist, E. Petrini, H. Malm, J. Borglind, S. Smuk, H. Pettersson, J. Y. Andersson, Nanotech Northern Europe, March 27-29 2007, Helsinki, Finland, Oral presentation.

Study of the performance and voltage mediated tuning of the detection wavelength in Quantum Dots-in-a-Well Infrared Photodetectors
L. Höglund, P. O. Holtz, C. Asplund, Q. Wang, S. Almqvist, E. Petrini, H. Malm, J. Borglind, S. Smuk, H. Pettersson, J. Y. Andersson, Low Dimensional Structures and Devices, April 15-20 2007, San Andrés, Colombia, Oral presentation.

Tunability in the Detection Wavelength of a Quantum Dots-in-a-Well Infrared Photodetector
L. Höglund, P. O. Holtz, C. Asplund, Q. Wang, S. Almqvist, E. Petrini, H. Pettersson, J. Y. Andersson, Quantum dot meeting at Imperial College, London, Jan 2008, BEST POSTER PRESENTATION !!!

Tunability in the Detection Wavelength of a Quantum Dots-in-a-Well Infrared Photodetector
L. Höglund, P. O. Holtz, C. Asplund, Q. Wang, S. Almqvist, E. Petrini, H. Malm, H. Pettersson, J. Y. Andersson, 5th International Conference on Semiconductor Quantum Dots, Gyeongju, Korea, May 2008, Poster.

Tuning of the detection wavelength in quantum dots-in-a-well infrared photodetectors
L. Höglund, P. O. Holtz, C. Asplund, Q. Wang, S. Almqvist, E. Petrini, H. Malm, H. Pettersson, J. Y. Andersson, SPIE Defence and Security, March 17-20 2008, Orlando, USA, Oral presentation, Paper iv.

Dual source optical pumping experiments revealing the origin of low temperature photocurrent peaks in Quantum Dots-in-a-Well Infrared Photodetectors, *L. Höglund, P. O. Holtz, C. Asplund, Q. Wang, S. Almqvist, E. Petrini, H. Malm, H. Pettersson, J. Y. Andersson*, International Conference on the Physics of Semiconductors (ICPS) - 29, July 27th - August 1st 2008, Rio de Janeiro, Brazil, Poster.

Acknowledgements

First of all I would like to thank my supervisor Per Olof Holtz at Linköping University for giving me the opportunity to work in this interesting field and for always keeping the door open, ready for discussions.

I am very grateful to my mentor Jan Andersson at Acreo, for trusting me with this challenging research, and for sharing his deep knowledge in physics and infrared technology with me.

I would also like to thank my additional supervisors, Mattias Hammar at KTH, Stefan Olsson and Stefan Johansson, FLIR systems, for showing such interest in my work and for making me see the problems from a different point of view.

My sincere gratitude to Håkan Pettersson, for always welcoming me with open arms to Halmstad and Lund, for measurements and interesting discussions, whenever I have trouble with my own equipment.

My profound thanks to Carl Asplund, Hedda Malm, Jan Borglind and Smilja Becanovic for teaching me and supporting me in the MOVPE growth.

A big hug goes to Qin Wang and Susanne Almqvist, for all the fabrication support of the QDIP-components and for always giving my components highest priority, helping me as soon as I ask for it!

Thank you Erik Petrini, for providing me with all the nice AFM micrographs and for the happy collaboration when studying the quantum dots.

Thanks also to Lassana Ouattara for the interesting collaboration, when studying the quantum dot structures with X-STM.

I would like to thank Mats Larsson and Björn Magnusson at IFM, for introducing me to the FTIR lab and Andreas Gällström for keeping the equipment in shape. Thanks also to Arne Eklund for all the technical assistance.

Thank you, Arvid Larsson and Fredrik Karlsson for your calm and patience when helping me out with new challenging experiments!

A special thanks goes to Staffan Hellström and Oscar Gustafsson for an inspiring collaboration in finding new detector concepts for IR detectors.

My appreciation to Bertrand, Teresita, Stéphane and all other nice colleagues at Acreo, for always encouraging me and supporting me, whenever I need.

This PhD study would not be possible without funding. I would like to express my gratitude to the Knowledge Foundation and the Swedish Foundation for Strategic Research for support grants and the Swedish Agency for Innovation Systems and the IMAGIC centre of excellence for financial support.

My enormous gratitude to Ingrid Bergman for wrapping this thesis in such a beautiful, colourful cover.

Thanks also to all my friends, who make my life outside work enjoyable!

To my encouraging family, for always being there for me, my solid support. I am especially grateful to my sister and her family, for sheltering me the first two years of my studies :)

To Henrik, my love, for showing such patience with my late working hours and for comforting me when things don't work.

Contents

CHAPTER 1

Introduction

Nanotechnology is a rapidly increasing field of science, with high potential for future industrial developments. Nanotechnology covers many disciplines ranging from medicine to electronics, with applications such as new drug delivery methods, improved imaging systems and quantum cryptography. The unifying theme is achievement of controlled fabrication of materials, in which the functionality is based on structures with dimensions between 1 and 100 nm. When a material is reduced in size to these dimensions, new physical phenomena may occur, which can be used to enhance the properties of the material.

In the field of nanoelectronics, quantum mechanical effects are of great importance for the properties of materials and devices. These are the governing effects in low dimensional structures, such as quantum wells (QWs), quantum wires (QWRs) and quantum dots (QDs), in which the motion of electrons and holes is confined to 2 dimensions (2D), 1D and 0D, respectively. The spatial confinement acts to reduce the allowed energy levels of the charge carriers, which opens up new possibilities to tailor the electronic properties of the material. The first quantum structure of this kind was proposed by L. Esaki and R. Tsu [1] in 1970. They proposed a *superlattice* with thin layers (around 10 nm) of two alternating semiconductor materials, resulting in allowed and forbidden energy bands for charge carriers. They expressed the possibility to obtain "*a novel class of man-made semiconductors*" and in the years to follow, such quantum structures were indeed realised and devices using these structures were developed. Lasers and infrared detectors are two examples of successful devices using QWs. Further improvements of device performance are expected when the charge carriers are confined to even lower dimension, 1D or 0D, as

is the case in QDs. The improved performance is connected to the atom-like behaviour of charge carriers in QDs, which are restricted to discrete energy levels by the quantum effects. In infrared photodetectors, the discretised energy levels in QDs act to suppress the dark current, which enables higher operating temperatures [2]. Furthermore, QDs can absorb light at all angles of incidence, while QWs only can absorb light with the electric field polarized in the quantisation direction of the QW.

In contrast to real atoms, the energy level separation can be adjusted by the size, shape and composition of the QD. This fact can be used for tailoring the energy level scheme to match the needs for a given application. In QD infrared photodetectors, the energy separation between two adjacent energy levels is tuned for detection within the infrared wavelength region. Electrons situated in a lower energy state can then be excited to a higher energy state, by absorption of photons. The electrons in the excited state can be swept out of the QD by an applied bias and contribute to the photocurrent in the infrared detector. In the frame of this work, a more elaborate version of the QD-based infrared photodetectors with the QDs inserted in a QW layer, i.e. dots-in-a-well (DWELL), have been developed and studied. The detection wavelength is then partly determined by the dot and partly by the well, and an increased flexibility for tailoring of the detection wavelength is thereby achieved. The work in this thesis involves growth and characterisation of the QD based material, as well as characterisation of infrared detector components based on QDs. The studies are aiming at an increased understanding of the physical properties of these components.

CHAPTER 2

Semiconductors

2.1 Crystal structure

Most of the semiconductors used today are crystalline, i.e. the atoms are arranged in a periodic way. The building blocks of the crystal are called *unit cells* and the crystal lattice is constructed by a repetition of these unit cells. One such unit cell, called a *face-centered cubic* (fcc) unit cell, is illustrated in figure 2.1a. It has *lattice points* (available positions for atoms or molecules) at each corner of the cubic unit cell and also at the center of each face of the cube. This unit cell has special relevance to the III-V materials, indium arsenide (InAs) and gallium arsenide (GaAs) which have been studied in this work. GaAs and InAs are based on two interpenetrating fcc-lattices, displaced by $(a/4, a/4, a/4)$, where a is the *lattice constant* (the distance between two atoms specifying the size of the unit cell). This structure is called a *zinc-blende* structure (Fig. 2.1b).

2.2 Reciprocal lattice

When studying properties of semiconductors such as quantum mechanical properties of electrons, wave propagation in a crystal or the crystal structure of the material, it is very useful to use a reciprocal lattice instead of the real lattice. The reciprocal lattice is the corresponding Fourier domain to the real crystal lattice, where the lattice vectors $\mathbf{K}$ are wave vectors with the dimension of reciprocal length. The reciprocal lattice to the fcc-lattice in figure 2.1a is a

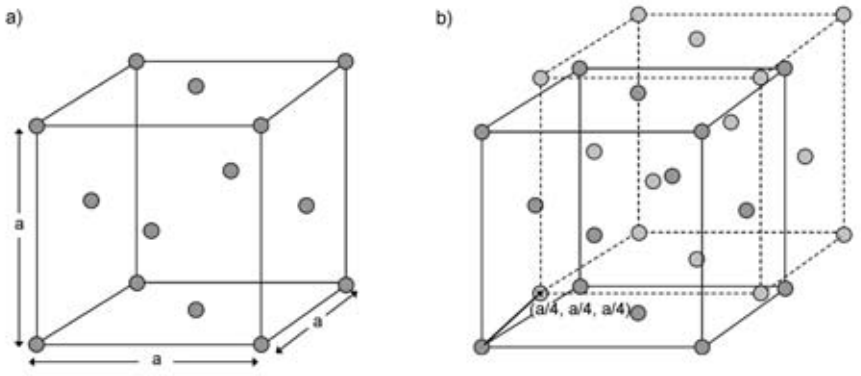

Figure 2.1: (a) fcc unit cell with lattice parameter a, the spheres represent lattice points, which can be occupied by atoms or molecules (b) zinc-blende structure, constructed by two fcc lattices displaced by (a/4, a/4, a/4).

body centered cubic (bcc) lattice (Fig. 2.2a), which has a lattice point at each corner and one lattice point in the centre of the cubic unit cell. From the reciprocal lattice, the first *Brillouin zone* can be extracted (Fig. 2.2b). This zone contains all the important information of the lattice and is therefore often used when discussing the electronic properties of a semiconductor. In figure 2.2, some important symmetry points are also shown (which are often referred to in these matters).

2.3 Electronic structure

Electrons bound to the core of an atom can not move arbitrarily, but are restricted to move in particular orbitals around the core of the atom, referred to as s, p, d and f orbitals, etc. This results in a discrete number of allowed energy levels of the electrons (Fig. 2.3a). When several identical atoms are brought together, electrons originating from different atoms will start to interact. The energy levels of the atoms then split, forming *energy bands* instead of discrete energy levels (Fig. 2.3b). The energy regions separating the energy bands are forbidden regions for electrons and are called *band gaps*. Since the energy bands are formed from the splitting of the atomic energy levels, the number of energy states within one band are proportional to the number of atoms (N) in the material. This relation can be expressed with the *density of states* per energy interval *g(E)* as in equation 2.1, where v_D is the degeneracy factor (= 2 for electrons).

$$v_D N = \int_{E_{min}}^{E_{max}} g(E)dE \tag{2.1}$$

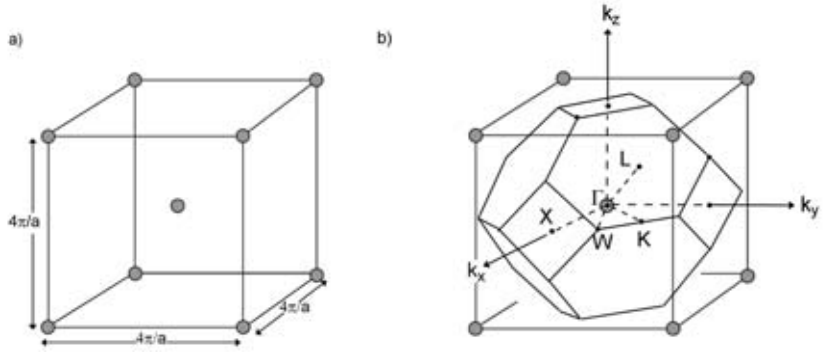

Figure 2.2: (a) Reciprocal lattice of a face-centered cubic lattice (which is a body-centered cubic lattice) (b) The first Brillouin zone, extracted from the reciprocal lattice. Some of the high symmetry points are marked: Γ (**k**=0), X (**k** = $\frac{2\pi}{a}\hat{x}$), L ($\frac{\pi}{a}(\hat{x}+\hat{y}+\hat{z})$), K ($\frac{3\pi}{2a}(\hat{x}+\hat{y})$), W ($\frac{\pi}{a}(2\hat{x}+\hat{y})$).

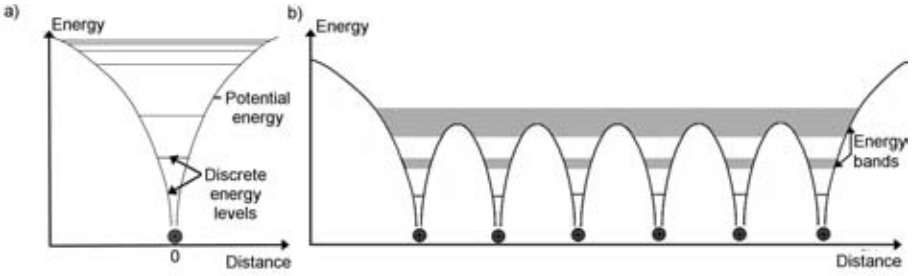

Figure 2.3: Potential energy of the electrons in (a) an atom with discrete allowed energy levels (b) a crystal with allowed energy bands.

Depending on the electron distribution in the energy bands and the size of the band gap, different properties of the material are obtained. If a band is only partly filled, the material has good electrical conductance since electrons are free to move to unoccupied states within the band. The material is then classified as a *metal*. If the highest occupied band is completely filled at a temperature of T = 0 K, the material has no electrical conductance at this temperature. However, depending on the size of the band gap, separating the highest occupied band (*valence band*) and the lowest unoccupied band (*conduction band*), the material can become conductive at higher temperatures due to thermal excitation of carriers to the conduction band. For narrow band gap materials this is the case, which is why they are called *semiconductors*. If the band gap is large, the probability for thermal excitation is too low and the material is classified as an *insulator*.

Electrons in crystalline semiconductors are strongly influenced by the periodic potential created by the atoms in the crystal. The corresponding electron wave function (ψ), referred to as a *Bloch function*, is the product of a function with the periodicity of the lattice, $u_k(\mathbf{r})$ (Eq. 2.2 and 2.3) and a plane wave acting as an envelope function. $\mathbf{k}$, $\mathbf{r}$ and $\mathbf{R}$ in equations (2.2) and (2.3) correspond to the wave vector, an arbitrary vector in real space and a lattice vector in real space, respectively. The wave vector $\mathbf{k}$ relates to the wavelength λ as: $|\mathbf{k}| = \frac{2\pi}{\lambda}$.

$$\psi_k(\mathbf{r}) = e^{i\mathbf{kr}} u_k(\mathbf{r}) \tag{2.2}$$

$$u_k(\mathbf{r}) = u_k(\mathbf{r} + \mathbf{R}) \tag{2.3}$$

The allowed energy bands of an electron as a function of the wave vector, $\mathbf{k}$, can be calculated using for example the tight-binding theory or the k.p-model. The energy dispersion is often displayed in an energy band diagram as shown for GaAs in figure 2.4a, for certain symmetry directions of the crystal (shown in figure 2.2b). From the band diagram, it can be seen that the conduction band minimum and the valence band maximum are located at the same point in the reciprocal space (the Γ-point). This makes GaAs a *direct band gap* material, which means that no interaction with *phonons* (lattice vibrations) are needed for optical transitions to occur. At the Γ-point there are two degenerate valence bands, corresponding to two different hole types; *heavy holes* (HH) and *light holes* (LH). At an energy distance Δ_{SO}, there is a *split-off* (SO) valence band (Fig. 2.4b).

The differences between the three valence band types are related to the symmetry of the Bloch wave functions. Whereas the conduction band exhibits s-like symmetry, the valence bands exhibit p-like symmetry. s- and p-like symmetry refer to the atomic picture of the electron wave functions, where a s-orbital is spherically symmetric around the nucleus of an atom, while a p-orbital is composed of two ellipsoids, which have a point of tangency at the nucleus.

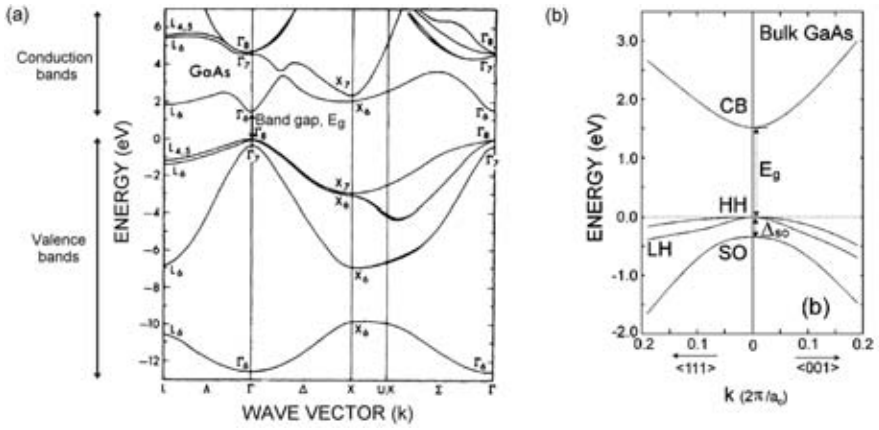

Figure 2.4: (a) Calculated energy band diagram of GaAs, with the conduction bands and valence bands and the band gap, E_g marked (b) Magnification of the band structure around the Γ point, showing the lowermost conduction band (CB) and the uppermost valence bands, including the heavy hole (HH), the light hole (LH) and the split off band (SO) [3].

As opposed to the s-like symmetry, p-like symmetry is highly anisotropic, as shown for p_z-orbitals in figure 2.5, where the wave functions overlap strongly in the z-direction and very weakly in the x- and y-directions. As a result of the anisotropy, the p-like bands have an orbital angular momentum, **l**, which have influence on the energy positions of the valence bands. The angular momentum of an electron arises due to its orbiting about the axis, defined by this vector ($\mathbf{l} = \mathbf{r} \times \frac{\hbar}{i}\nabla$). Since the electron is charged, the circulating current gives rise to a magnetic field. The energy of the electron is dependent on whether its spin (**S**) is aligned parallel or antiparallel to this field. This results in the energy separation Δ_{SO} between the bands.

The different hole states can be further specified, when investigating the quantisation properties of **l** and **s**. The component of **l** along, for example, the z-axis is quantised and can take the values: $l_z = \hbar$, 0, -$\hbar$, normally labeled with a quantum number $m = 1, 0, -1$. Using the m quantum numbers as base ($|m\rangle$), the different p-states can be expressed in terms of $|X\rangle$, $|Y\rangle$ and $|Z\rangle$, as in the equations (2.4).

$$\begin{aligned} |0\rangle &= |Z\rangle \\ |+1\rangle &= \sqrt{\frac{1}{2}}|X\rangle + i|Y\rangle \\ |-1\rangle &= \sqrt{\frac{1}{2}}|X\rangle - i|Y\rangle \end{aligned} \tag{2.4}$$

However, in order to fully describe the HH, LH and SO valence bands,

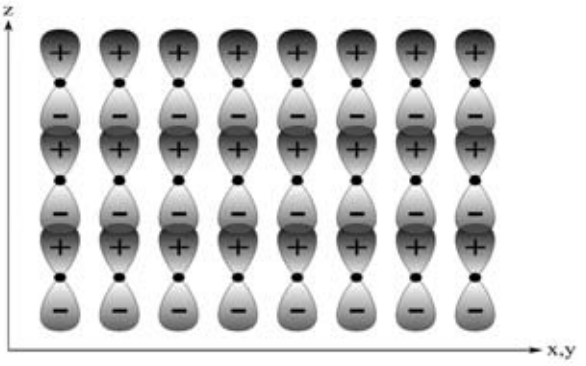

Figure 2.5: Schematic picture of p_z orbitals in a lattice.

the spin-orbit coupling must be included. This is achieved by calculating the total angular momentum, $\mathbf{j} = \mathbf{l} + \mathbf{s}$, which connects the spin and the orbital angular momentum. The corresponding spin along the z-axis can take the values $s_z = \frac{1}{2}\hbar, -\frac{1}{2}\hbar$, referred to as spin up ($\uparrow$) and spin down ($\downarrow$), respectively. Consequently, $\mathbf{j}$ may take the values $j = l + s = \frac{3}{2}\hbar$ or $j = l - s = \frac{1}{2}\hbar$, with the corresponding values of $j_z = \pm\frac{3}{2}, \pm\frac{1}{2}$. Finally the different hole states can be defined in terms of $|j, j_z\rangle$:

$$HH_1 = |\frac{3}{2}, +\frac{3}{2}\rangle = |+1\uparrow\rangle \tag{2.5}$$

$$HH_2 = |\frac{3}{2}, -\frac{3}{2}\rangle = |-1\downarrow\rangle \tag{2.6}$$

$$LH_1 = |\frac{3}{2}, +\frac{1}{2}\rangle = \sqrt{\frac{1}{3}}|+1\downarrow\rangle - \sqrt{\frac{2}{3}}|0\uparrow\rangle \tag{2.7}$$

$$LH_2 = |\frac{3}{2}, -\frac{1}{2}\rangle = -\sqrt{\frac{1}{3}}|-1\uparrow\rangle - \sqrt{\frac{2}{3}}|0\downarrow\rangle \tag{2.8}$$

$$SO_1 = |\frac{1}{2}, +\frac{1}{2}\rangle = \sqrt{\frac{2}{3}}|+1\downarrow\rangle + \sqrt{\frac{1}{3}}|0\uparrow\rangle \tag{2.9}$$

$$SO_2 = |\frac{1}{2}, -\frac{1}{2}\rangle = -\sqrt{\frac{2}{3}}|-1\uparrow\rangle + \sqrt{\frac{1}{3}}|0\downarrow\rangle \tag{2.10}$$

These equations, in combination with $|S\rangle$ representing the conduction band electrons, serve to describe the energy bands closest to the band gap. This representation is used to clarify which optical transitions occur between the different energy bands in a semiconductor. This is described in more detail in section 2.6.

2.4 Dimensionality of the density of states

In the previous section, the electronic structure in a bulk semiconductor was described. An electron in bulk material was represented by a Bloch wave function, consisting of the periodic part associated with the atomic positions, times a plane wave. The plane wave description means that the position of an electron is not determined, i. e. the probability of finding the electron anywhere in space is equal. However, if there is an outer restriction to the movement of the electron, the plane wave description can no longer be used. If the electron motion is restricted to a thin layer, a so called *quantum well*, an envelope function description is used in the direction of restriction (here z-direction). The resulting wave function is given by equation (2.11), where C is a normalisation constant, $\phi(z)$ is the quantum well envelope function and $u(\mathbf{r})e^{i\mathbf{k}_{x,y}\mathbf{r}_{x,y}}$ is the Bloch wave function, where the plane wave is restricted to the x,y-plane. When further reducing the degrees of freedom to 1D (*quantum wire*) and 0D (*quantum dot*), the electron wave function is further influenced, as shown in equation (2.12) and (2.13), respectively.

$$\psi_{2D}(\mathbf{r}) = Cu(\mathbf{r}_{x,y,z})\phi(z)e^{i\mathbf{k}_{x,y}\mathbf{r}_{x,y}} \quad (2.11)$$

$$\psi_{1D}(\mathbf{r}) = Cu(\mathbf{r}_{x,y,z})\phi(y,z)e^{i\mathbf{k}_{x}\mathbf{r}_{x}} \quad (2.12)$$

$$\psi_{0D}(\mathbf{r}) = C\phi(x,y,z)u(\mathbf{r}_{x,y,z}) \quad (2.13)$$

This change of character of the wave function, also has an influence on the density of k-states (or related energy states). In a bulk material (3D), the allowed k-values are illustrated in Fig. 2.6, where each k-value can be occupied by two electrons (with spin up and spin down). It is evident from the wave function descriptions (equations 2.2, 2.11 - 2.13) that the k-space reduces from 3D to 0D along with the reduced degree of freedom of the electron. Consequently, the density of states also changes with reduced dimensionality. Whereas the density of states for a bulk semiconductor is proportional to the square root of the energy (Fig. 2.7a), the density of states in the 2D case exhibits a step-like behaviour vs the energy (Fig. 2.7b) and for 1D and 0D structures, the density of states concentrates to specific energies (Fig. 2.7c, d). Limitations of the degrees of freedom can be established by creating potential barriers for the charge carriers which act to restrict the motion of the carriers. The realization of these structures is described in more detail in section 2.5.

2.5 Quantum structures

When combining different semiconductor materials in so-called *hetero-structures*, a material with novel optical and/or electronic properties can be obtained. When two different materials are brought together, their band gaps are aligned. The band gap alignment can introduce potential barriers and traps

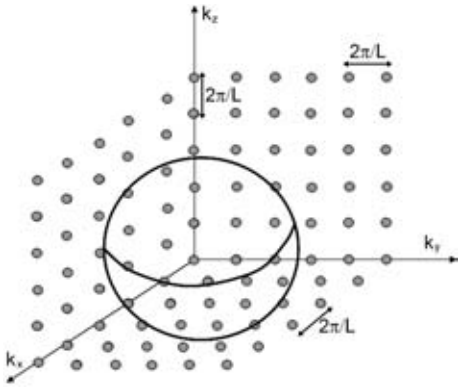

Figure 2.6: Allowed k-values in a bulk semiconductor material. The spacings between the allowed k-values, $\frac{2\pi}{L}$, are related to the size of the material (L^3).

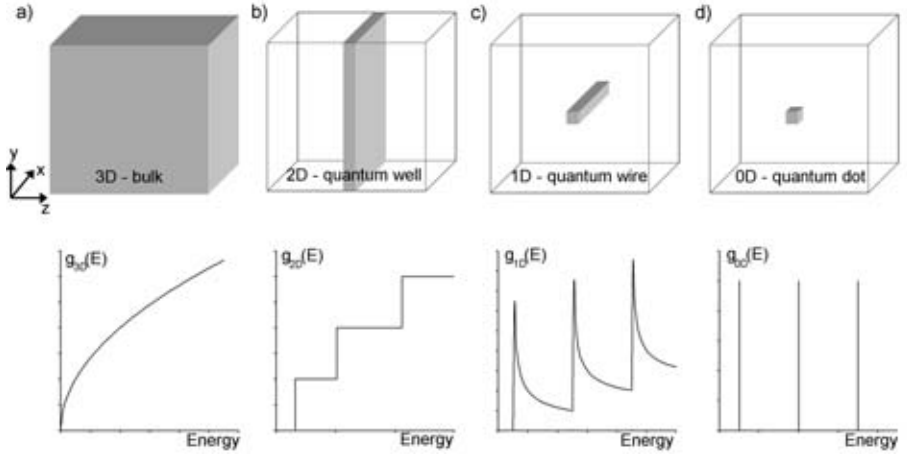

Figure 2.7: Density of states (g(E)) for structures of different dimensionalities: (a) bulk: $g_{3D}(E) = \frac{m\sqrt{2mE}}{\pi^2\hbar^3}$ (b) quantum well: $g_{2D}(E) = \frac{m}{\pi\hbar^2}$ (c) quantum wire: $g_{1D}(E) = \frac{1}{\pi\hbar}\sqrt{\frac{2m}{E}}$ (d) quantum dot: $g_{0D}(E) = \delta(E - E_n)$.

for the charge carriers, which cause restrictions of the carrier motion. Three types of band gap alignments can be distinguished; type I, type II and type III (see figure 2.10). In the case of type I band alignment, both electrons and holes are trapped in the narrow band gap material, while in a type II band alignment, only one type of charge carrier is trapped. In type III heterostructures, the band gaps are staggered, which gives the peculiar situation that the valence band edge of one semiconductor has higher energy than the conduction band edge of the other semiconductor. Heterostructures can be realized by atomically controlled growth of semiconductor layers with different compositions (see chapter 3). Two different realizations of heterostructures are described in section 2.5.2 and 2.5.3.

2.5.1 Strained layers

When combining different semiconducting layers in heterostructures, it is sometimes "convenient" to grow materials with similar lattice constants, such as aluminum gallium arsenide ($Al_xGa_{1-x}As$) and GaAs or a compound of indium gallium arsenide with 53 % indium ($In_{0.53}Ga_{0.47}As$) and indium phosphide (InP) (Fig. 2.8). The reason for this is that thick layers can be grown with very high crystalline quality, since there are no built-in forces in the structure, which can give rise to dislocations. However, in order to enable designs of materials with specific properties it could be necessary to combine non lattice-matched materials. During growth, the non lattice matched layer is forced to adjust its lattice constant (a_l) to adopt to the lattice constant of the substrate (a_s), see Fig. 2.9. This causes strain in the layer (ϵ), which in the lateral direction (perpendicular to the growth direction) is given by equation (2.14). The strain can be either compressive or tensile, depending on whether the lattice consant of the layer is larger or smaller than the lattice constant of the substrate (Fig. 2.9). The adjustment of the lattice constant in the lateral direction is accompanied by a change of the lattice constant in the growth direction. If there is a compressive strain, which forces the lattice constant to reduce in the lateral direction, the lattice constant in the growth direction increases and vice versa for tensile strain. The resulting strain in the growth direction (ϵ_{zz}) is related to the lateral strain via the elastic constants, C_{11} and C_{12} for a cubic material (eqn. 2.15). The strain energy in the layer increases with increasing thickness and this limits the thickness of the layer. If the accumulated strain becomes too large, this energy can be released either by formation of dislocations or, if the growth conditions are right, by formation of dislocation free islands, so called quantum dots. The distortion of the lattice in strained layers also influences the energy band structure. The degeneracy of light and heavy holes at the Γ-point is lifted and the energy levels are shifted as a result of the strain. The average shift of the conduction and the valence band edges for a strained layer can be calculated using the equations (2.16) and (2.17), where a_c and a_v correspond to the deformation potentials of the conduction and valence

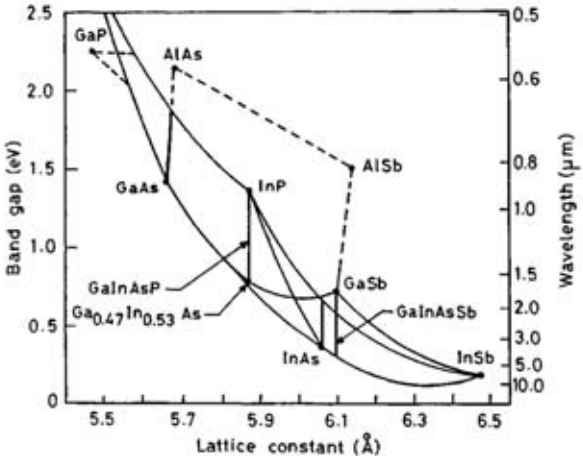

Figure 2.8: Diagram of band gaps and lattice constants for semiconductors in the III-V-group.

Table 2.1: Material parameters for different III/V-materials

	Deformation potentials		Lattice constant	Elastic constants	
Material	a_c [eV]	a_v [eV]	a [Å]	C_{11} [GPa]	C_{12} [GPa]
GaAs	-7.17	-1.16	5.653	1221	566
InAs	-5.08	-1.00	6.058	832.9	452.6
AlAs	-5.64	-2.47	5.661	1250	534
InP	-6.0	-0.60	5.870	1011	561

band, respectively [4]. The material parameters needed for calculating of the band edge shifts for different III/V-materials are given in table 2.1 [5].

$$\epsilon_{xx} = \epsilon_{yy} = \frac{a_s - a_l}{a_l} \tag{2.14}$$

$$\epsilon_{zz} = -2\frac{C_{12}}{C_{11}}\epsilon_{xx} \tag{2.15}$$

$$\Delta E_c = a_c(\epsilon_{xx} + \epsilon_{yy} + \epsilon_{zz}) \tag{2.16}$$

$$\Delta E_v = a_v(\epsilon_{xx} + \epsilon_{yy} + \epsilon_{zz}) \tag{2.17}$$

2.5.2 Quantum wells

A quantum well (QW) is a heterostructure of type I or type II (Fig. 2.10), consisting of a thin layer of a semiconducting material surrounded by another

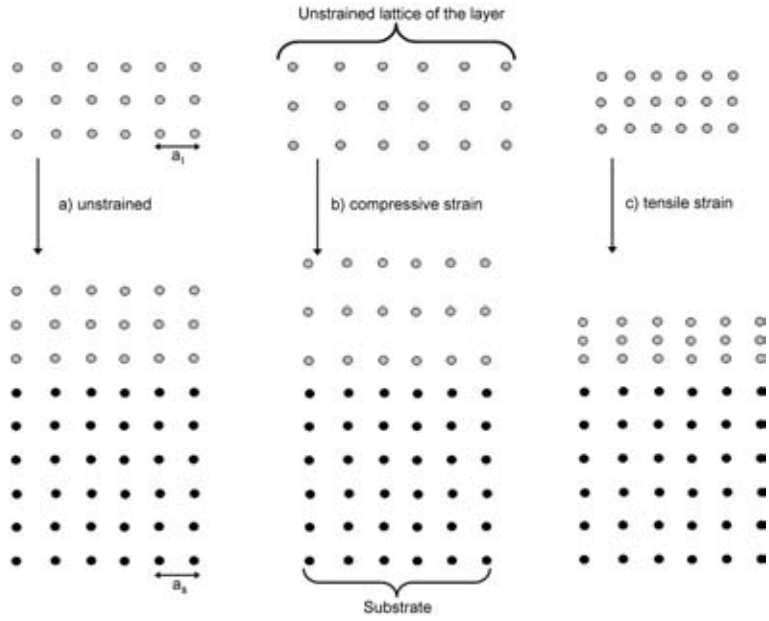

Figure 2.9: Schematic illustration of the influence on the lattices in heterostructures for (a) lattice matched layers (b) lattice mismatched layers, when the lattice constant of the film is larger than that of the substrate (c) lattice mismatched layers, when the lattice constant of the film is smaller than that of the substrate.

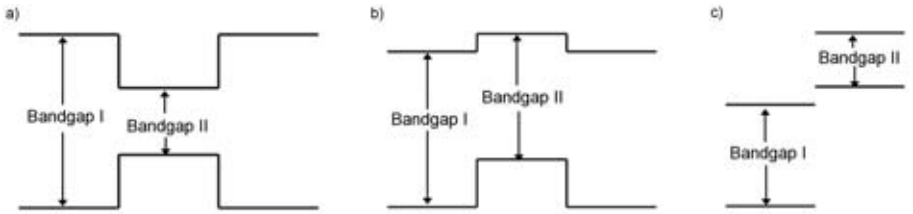

Figure 2.10: Different possibilities of band gap alignments a) type I - a narrower band gap (band gap II) is enclosed within the wider band gap (band gap I) b) type II - band gap II is partly enclosed within band gap I and partly outside band gap I c) type III - the band gaps are not overlapping at all

semiconducting material with a wider band gap than the QW itself. The QW then acts as a potential well, where electrons and/or holes no longer can move freely in one direction (the z-direction in figure 2.7b). The electron wave function is described by an envelope function (ϕ) in this direction (Eq. 2.11) and since the envelope function must obey the boundary conditions, there is a finite set of resonant envelope functions allowed (Fig. 2.11b). The corresponding allowed energies can be calculated with the Schrödinger equation, which is the energy conservation equation for waves;

$$(-\frac{\hbar^2}{2m^*} + V(z))\phi(z) = \varepsilon\phi(z) \tag{2.18}$$

where $\hbar$ is Planck's constant divided by 2π and m^* is the electron effective mass. The first term on the left hand side in this equation corresponds to the kinetic energy, the second term to the potential energy and the right hand side corresponds to the total energy. The solutions to the Schrödinger equation for a quantum well are of the form $\varepsilon_n + \hbar^2(k_x^2 + k_y^2)/2m$ (n=1, 2, 3...), where the first term corresponds the discrete energy values obtained from the quantisation in the z-direction and the second term corresponds to the free electron energies in the x-y-direction (visualised in Fig. 2.11).

The confinement of the wave functions in one direction also gives rise to a polarisation dependence of the hole states. If the growth direction is defined in the z-direction and the angular momentum j_z is parallell to z, the heavy holes are described by $|X\rangle \pm i|Y\rangle$. $\mathbf{u}(r)$ (Eq. 2.3) of the heavy holes are thus oriented solely in the x,y-plane, while light holes (equations 2.7 and 2.8) will have significant contributions also in the z-direction.

2.5.3 Quantum dots

If the thin layer forming a QW is further reduced in dimensionality to a small box or a small island, a quantum dot (QD) is obtained. The potential barrier

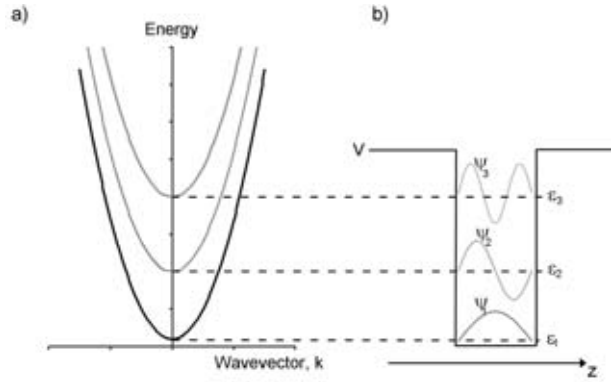

Figure 2.11: Solutions to the Schrödinger equation in a quantum dot with confinement in the z-direction and an energy barrier height V. (a) The dispersion of energy vs the wave vector, k_x or k_y (b) Eigenvalues ϵ_1, ϵ_2 and ϵ_3, with the corresponding wave functions ψ_1, ψ_2 and ψ_3.

surrounding the QD restricts the energy of the carriers trapped inside the dot to discrete energy levels (ε_n, n=1, 2, 3...), similar to the discrete energies allowed for electrons in an atom. Due to this similarity, QDs are sometimes called *artificial atoms*. The probability densities ($\psi^*\psi$) corresponding to the allowed energy levels of electrons and holes are visualised in figure 2.12. This shows that the electrons and holes are strongly localised to the QD. The symmetries of the wave functions resembles the symmetry of wave functions in an atom (s, p, d, f...). The ground state of a QD has an s-like shape, while the shapes of the wave functions of the first excited states are p-like, etc. As in an atom, there is a limitation of the number of charge carriers, which can occupy each state. The ground state (s) and the first excited states (p_x and p_y, respectively) can each hold two electrons (with spin up and spin down).

Similarly to the case of the QW, the periodic heavy hole Bloch functions are oriented in the lateral direction of the QD, while a significant contribution of the light holes is oriented in the vertical direction (growth direction) of the QD. This introduces a polarization dependence also in the QDs.

Coulomb charging

The electrostatic interaction between carriers captured in a QD is significant, due to the close proximity of the charge carriers. For each additional charge carrier (of the same polarity), the total energy of the carriers increases by an amount ΔE_{ee} (or ΔE_{hh} in the case of holes). The charging energy can be obtained from the capacitance of the QD, C_{QD} according to equation (2.19). The QD-capacitance for a QD can be estimated by a capacitance of a disk with the radius r (equation 2.20).

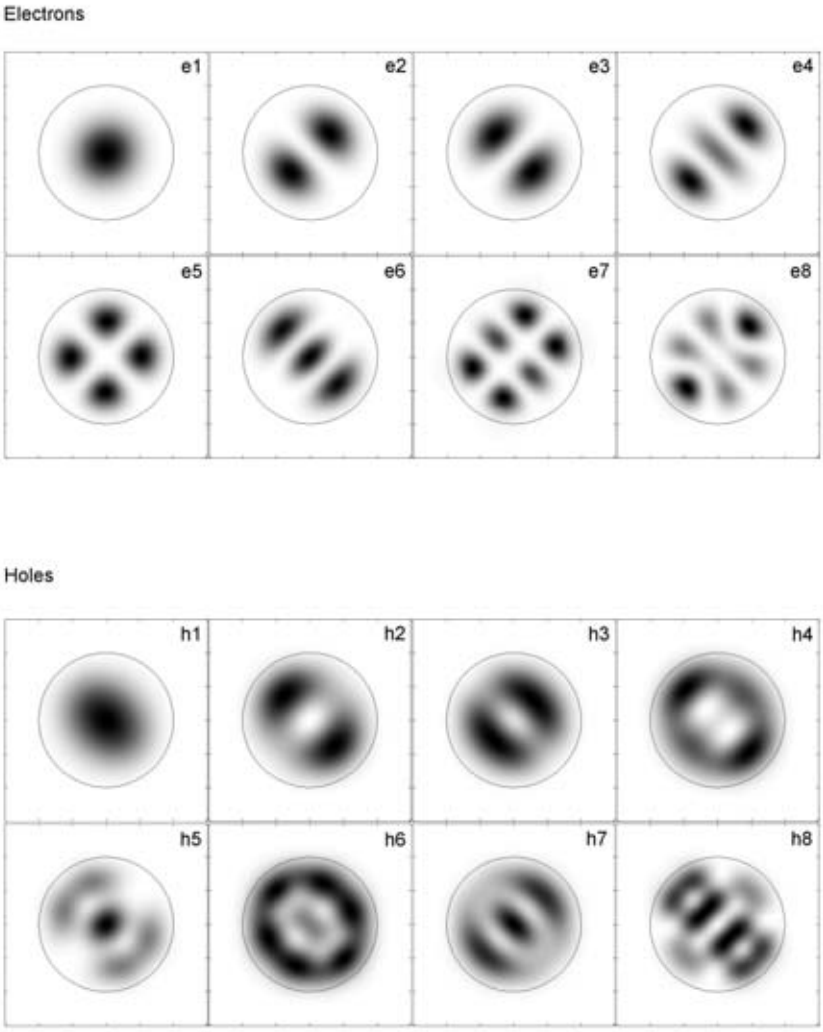

Figure 2.12: Probability density functions (projected onto a plane) for electrons and holes in a lens-shaped InAs/GaAs QD, corresponding to the discrete energy levels $e_1 - e_8$ for electrons and $h_1 - h_8$ for holes. The width and height of the simulated QD is 20 and 3.5 nm, respectively.

$$\Delta E_{ee} = \frac{q^2}{C_{QD}} \tag{2.19}$$

$$C_{QD} = 8\epsilon_0\epsilon_{r,matrix}r \tag{2.20}$$

For an InAs/GaAs QD with a radius of 8 nm, the charging energy is approximately 20 meV [7]. However, if the charge carriers captured in the QD have different polarity, the total energy decreases due to the attractive forces between electrons and holes. This energy (ΔE_{eh}) is then approximately the same as the charging energy.

2.6 Optical properties

Electronic transitions between different energy states in a semiconductor can occur through absorption or emission of photons. These properties can for instance be utilized in the design of photon detectors or light emitting devices. A boundary condition for these transitions to occur is that the total energy and momentum should be conserved. The momentum of a photon is very small in comparison with the electron momentum, which is why it can be neglected. Depending on the photon energy, different transitions are enabled. Two different optically induced transitions can be distinguished: interband and intersubband transitions.

The main ingredience when calculating the probability of an optical transition is the matrix element, which describes the interaction between the wave functions of two states. The matrix element for an optical transition between two states is given by equation (2.21):

$$\langle f\mathbf{k}'|\mathbf{e}\cdot\hat{\mathbf{p}}|i\mathbf{k}\rangle = \int \psi^*_{f\mathbf{k}'}(\mathbf{r})\mathbf{e}\cdot\hat{\mathbf{p}}\psi_{i\mathbf{k}}(\mathbf{r})d^3\mathbf{r} \tag{2.21}$$

where f and i represent the wave functions (ψ) of the final and initial states at wave vectors $\mathbf{k}'$ and $\mathbf{k}$, respectively. $\mathbf{e}$ is the polarization vector and $\hat{\mathbf{p}}$ is the momentum operator ($=-i\hbar\nabla$). The matrix element is derived for the special cases of bulk material transitions as well as transitions in quantum structures (2.6.1).

2.6.1 Interband transitions

Interband transitions refer to transitions between the valence band and the conduction band and can include either absorption or emission of photons. In the case of absorption, the photon energy is used to excite an electron from the valence band to the conduction band and when electrons and holes are situated

in a close proximity to each other, they can recombine again under the emission of a photon.

Bulk interband transitions

The wave function in bulk material is described by the Bloch function, $u(\mathbf{r})e^{i\mathbf{kr}}$ (Eq. 2.2). In order to calculate the interband absorption, the wave functions of the conduction band (c) and the valence band (v) are inserted into the matrix element (2.21), resulting in equation (2.22):

$$\langle c\mathbf{k}'|\mathbf{e}\cdot\hat{\mathbf{p}}|v\mathbf{k}\rangle = \frac{1}{\Omega}\int u^*_{c\mathbf{k}'}(\mathbf{r})e^{-i\mathbf{k}'\mathbf{r}}\mathbf{e}\hat{\mathbf{p}}u_{v\mathbf{k}}(\mathbf{r})e^{i\mathbf{kr}}d^3\mathbf{r} \quad (2.22)$$

$$\langle c\mathbf{k}'|\mathbf{e}\cdot\hat{\mathbf{p}}|v\mathbf{k}\rangle = \frac{1}{\Omega}\mathbf{e}\int u^*_{c\mathbf{k}'}(\mathbf{r})e^{i(\mathbf{k}-\mathbf{k}')\mathbf{r}}[\hbar\mathbf{k}u_{v\mathbf{k}}(\mathbf{r})+\hat{\mathbf{p}}u_{v\mathbf{k}}(\mathbf{r})]d^3\mathbf{r} \quad (2.23)$$

where Ω is the volume of the material. $\hat{\mathbf{p}}$ operates with a first derivative on both the plane wave part and the periodic part (u_v) of the valence band wave function, which results in equation (2.23).

The integral of the first term in the square bracket vanishes, since it results in two orthogonal states. The remaining integral also is zero, unless $\mathbf{k}=\mathbf{k}'$, which leaves us with the matrix element of u($\mathbf{r}$) (equation (2.24)). The integral can be reduced to the volume over a unit cell (Ω_{cell}), since $u(\mathbf{r})$ is periodic between the unit cells.

$$\langle u_{c\mathbf{k}}|\mathbf{e}\cdot\hat{\mathbf{p}}|u_{v\mathbf{k}}\rangle = \frac{1}{\Omega_{cell}}\int_{cell} u^*_{c\mathbf{k}}(\mathbf{r})\mathbf{e}\cdot\hat{\mathbf{p}}u_{v\mathbf{k}}(\mathbf{r})d^3\mathbf{r} \quad (2.24)$$

The periodic part of the Bloch functions u_c and u_v can be described in terms of $|S\rangle$ for the conduction band states and $|X\rangle$, $|Y\rangle$ and $|Z\rangle$ for the valence band states, as was described in section 2.3. With polarisation in the x-, y-, and z-directions, the operator reduces to p_x, p_y and p_z, respectively. The non-vanishing matrix elements are: $\langle S|p_x|X\rangle$, $\langle S|p_y|Y\rangle$ and $\langle S|p_z|Z\rangle$, which all equal $\frac{im_0P}{\hbar}$. P is a material-dependent parameter, which can be related to the effective mass as $\frac{1}{m_e}\approx 1+(\frac{2m_0P^2}{\hbar^2E_g})$.

Interband transitions in quantum structures

In order to calculate the matrix element for interband transitions in QWs or QDs, the wave functions described in the equations (2.11) and (2.13) are used, i.e. an envelope function $\phi(\mathbf{r})$ associated with the QW/QD as well as the Bloch function at the Γ-point, $u_{n0}(\mathbf{r})$. The plane waves give the condition that the k-vectors of the final and initial states need to be identical, as seen in equation (2.23). Using the normalised wave function $\psi(R)=\Omega^{\frac{1}{2}}\phi(\mathbf{r})u_{n0}(\mathbf{r})$, the matrix element is given by:

$$\langle f|\mathbf{e}\cdot\hat{\mathbf{p}}|i\rangle = \Omega\int \phi_c^*(\mathbf{r})u_c^*(\mathbf{r})(\mathbf{e}\cdot\hat{\mathbf{p}})\phi_v(\mathbf{r})u_v(\mathbf{r})d^3\mathbf{r} \tag{2.25}$$

The envelope function ϕ is a slowly varying function, as compared to the Bloch function, which varies within each unit cell. Consequently, equation (2.25) can be rewritten into a sum of integrals over the volume of a unit cell. In this interval, ϕ can be considered to be constant and can be pulled out of the integral as in equation (2.26):

$$\langle f|\mathbf{e}\cdot\hat{\mathbf{p}}|i\rangle \approx \Omega\sum_j^{cells}\phi_c^*(\mathbf{r_j})\phi_v(\mathbf{r_j})\int_{cell,j} u_c^*(\mathbf{r})(\mathbf{e}\cdot\hat{\mathbf{p}})u_v(\mathbf{r})d^3\mathbf{r} \tag{2.26}$$

The integral over each unit cell in equation (2.26) can be identified as the matrix element between the conduction band and valence band Bloch functions, $\langle u_{c\mathbf{0}}|\mathbf{e}\cdot\hat{\mathbf{p}}|u_{v\mathbf{0}}\rangle$, and the sum of ϕ-functions can again be rewritten into an integral (see equation 2.27).

$$\langle f|\mathbf{e}\cdot\hat{\mathbf{p}}|i\rangle \approx \langle u_{c\mathbf{0}}|\mathbf{e}\cdot\hat{\mathbf{p}}|u_{v\mathbf{0}}\rangle\int \phi_c^*(\mathbf{r})\phi_v(\mathbf{r})d^3\mathbf{r} \tag{2.27}$$

The matrix element has thereby been separated into two parts, one involving the Bloch wave functions and the polarisation of the incoming light and one involving the QW envelope wave functions. The selection rules emanating from these two parts are now investigated:

- **Polarisation dependence**
  From the matrix element of the Bloch wave functions $\langle u_c|\mathbf{e}\cdot\hat{\mathbf{p}}|u_v\rangle$, a polarisation dependence of the interband absorption can be deduced. As was described in section 2.5.2, the orientation of the heavy hole states is solely in the x,y-plane (HH1=$\sqrt{\frac{1}{2}}(|X\uparrow\rangle + i|Y\uparrow\rangle)$), while the light hole states have a significant contribution in the z-direction (LH1=$\sqrt{\frac{1}{6}}(|X\downarrow\rangle + i|Y\downarrow\rangle) - \sqrt{\frac{2}{3}}|Z\uparrow\rangle$). This sets a restriction on the polarisation of light to be absorbed. If the light is polarised in the x- or y-direction, the matrix elements are reduced to $\langle u_c|p_x|u_v\rangle$ or $\langle u_c|p_y|u_v\rangle$. The remaining non-zero matrix elements are then $\langle S|p_x|X\rangle$, $\langle S|p_y|Y\rangle$ ($=\frac{im_0P}{\hbar}$). This enables absorption by heavy holes as well light holes. However, if light is polarised in the z-direction, the only none-zero matrix element is $\langle S|p_z|Z\rangle$. An interband transition is then only possible if light holes are involved. These facts can be used to distinguish between transitions emanating from heavy holes or light holes. For transitions from a LH state, for example $|\frac{3}{2},\frac{1}{2}\rangle = \sqrt{\frac{1}{6}}(|X\downarrow\rangle + i|Y\downarrow\rangle) - \sqrt{\frac{2}{3}}|Z\uparrow\rangle$, the matrix element is twice as large for light polarized in the z-direction

compared to light polarized in the x-direction. For transitions from a HH state, the matrix element is zero for light polarized in the z-direction and non-zero for light polarized in the x- or y-direction.

- **Envelope wave function overlap**
  The part of the matrix element involving the QW/QD envelope functions is an overlap integral between the envelope functions in the conduction band and the valence band, respectively. These envelope functions are symmetric or antisymmetric, depending on the quantum number, n, of the wave functions (see figure 2.11 for conduction band wave functions). The largest overlap is achieved if both envelope functions have the same quantum number n. If the envelope functions have different parity, the overlap is zero.

The two above conditions both need to be fulfilled in order to induce an interband transition.

2.6.2 Intersubband transitions

An intersubband transition occurs between different subbands within either the conduction band or the valence band, involving excitation or relaxation of either electrons or holes. Intersubband transitions are especially relevant in heterostructures, where the energy of the transition can be tailored by the dimensions and the composition of the combined materials.

Intersubband transitions in quantum wells

The intersubband transitions in a quantum well is highly polarization-dependent, as will be demonstrated. The wave function for a quantum well, quantised in the z-direction, can be described by an envelope function $\phi(z)$ in the z-direction and a plane wave in the $\mathbf{r} = (x, y)$-directions:

$$\Psi_{i\mathbf{k}}(\mathbf{r}, z) = A^{-\frac{1}{2}}\phi(z)exp(i\mathbf{kr}) \tag{2.28}$$

If the polarization vector $\mathbf{e}$ is directed along the x-axis (in the plane of the QW), $\mathbf{e} \cdot \hat{\mathbf{p}} = -i\hbar\partial/\partial x$, operating on the initial state (i), only affects the plane wave. Consequently the matrix element is zero since the states i and j are orthogonal (equation 2.29) and there is no absorption of the light polarized in the x- or y-direction.

$$\langle f\mathbf{k}'|\hat{p}_x|i\mathbf{k}\rangle = \hbar k_x\langle f\mathbf{k}'|i\mathbf{k}\rangle = 0 \tag{2.29}$$

On the other hand, if $\mathbf{e}$ is directed in the z-direction (perpendicular to the QW), the operator $\mathbf{e} \cdot \hat{\mathbf{p}} = -i\hbar\partial/\partial z$ affects the envelope function of the bound state and the matrix element is given by:

$$\langle f\mathbf{k}'|\hat{p}_z|i\mathbf{k}\rangle = \frac{1}{A}\int dz \int d^2\mathbf{r}\phi_f^*(z)e^{i(\mathbf{k}-\mathbf{k}')\mathbf{r}}\hat{p}_z\phi_i(z) \tag{2.30}$$

The integral over $\mathbf{r}$ is zero, unless for $\mathbf{k} = \mathbf{k}'$, when it sums up to A. The integral in z can be written in terms of a matrix element (2.31), which can be used to calculate the absorption of the incoming light.

$$\langle f|\hat{p}_z|i\rangle = -i\hbar \int \phi_f^*(z)\frac{\partial\phi_i(z)}{\partial z}dz \tag{2.31}$$

The intersubband transitions of highest probability can be identified from equation (2.31) as transitions between energy states with large overlap integrals between the wave function of the final state and the derivative of the wave function of the initial state. This favours transitions from odd to even energy states, while the probability is very low for transitions between two odd or two even energy states.

Intersubband transitions in quantum dots

The strong polarization dependence of the absorption in quantum wells is due to the different properties of the wave function in the confinement direction (z) compared to the plane of the quantum well (x,y). In a quantum dot, the wave function is described by an envelope function $\phi(x, y, z)$ in all three space dimensions (compare with equation 2.28), which enables absorption of light polarized in any direction.

2.6.3 Excitons

The negative electron and the positive hole are attracted to each other, due to the opposite charges and can bind together, forming *excitons*. The bound state of an exciton is energetically positioned below the band gap of the host material. New optical transitions are thereby introduced, which act to modify the absorption edge. For low dimensional structures, optical transitions related to excitons are usually stronger than the corresponding continuum transitions. Consequently, excitonic transitions often dominate the absorption or emission spectra of these structures. In QDs, electrons and holes are already bound by the confinement in the dot, which makes exciton formation inevitable.

2.7 Phonons

At 0 K, all atoms in a lattice are positioned in their lowest energy position and no vibrations occur. As the temperature in the lattice increases, the thermal energy added is transformed to lattice vibrations. These lattice vibrations actually have quantised energies and the energy quanta are called *phonons*.

There are different kinds of atomic vibrations, either longitudinal (in-plane) or transverse to a plane. Phonons are further subdivided into optical and acoustical phonons depending on the properties of the vibrations.

Energy can be interchanged between phonons and electrons. Consequently, phonons play an important role in relaxation processes as well as in thermal excitation processes.

2.8 Electrical properties

2.8.1 Carrier transport

Carrier transport in a bulk semiconductor can be driven by e.g. drift or diffussion. Drift is caused by an electric field, while diffussion is driven by concentration gradients. In the presence of an electric field, carriers are accelerated by the field and the induced drift current is proportional to the electric field. As long as the field strengths are moderate, scattering limits the velocity of the carriers, which is reflected in the mobility of the carriers. At high electric field strengths, phonon generation reduces the velocity of the carriers, which eventually causes saturation of the velocity.

2.8.2 Quantum-confined Stark effect

In a quantum structure, the presence of an electric field tilts the band structure as well as shifts the energy levels. A bias-dependent shift of an energy level is referred to as a quantum-confined Stark shift. This effect is employed in electro-optical modulators, in order to modulate the reflection of incident light, but can also be used in infrared detectors to obtain tunability of the detection wavelength.

In symmetrical structures

The ground states in symmetrical quantum structures are subject to quantum-confined Stark shifts, with a quadratic field dependence ($\propto F^2$). This results in a relative lowering of the energy level of an electron (Fig 2.13) versus the holes. Excited energy levels, which still are well confined in the QW are almost unperturbed by the field. Consequently, an interband transition between ground states is red-shifted by the electric field, while intersubband transitions between the ground state and an excited state are blue-shifted compared to the unbiased case. The shift of the ground state level (ΔE_1) is given by equation (2.32):

$$\Delta E_1 = -C\frac{m^* q^2 F^2 L^4}{\hbar^2} \tag{2.32}$$

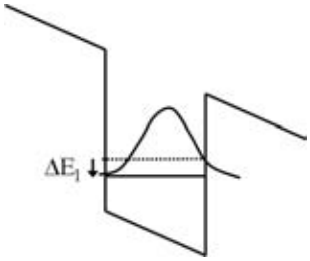

Figure 2.13: Stark shift, ΔE_1, of the ground state energy level in a square well.

where m^* is the effective mass, q the elementary charge, L is the width of the QW (or height in case of a QD) and C is a numerical constant (= 0.0022) [8].

The Stark shift of the ground state in a GaAs/AlGaAs QW is pronounced, with an increasing effect as the width of the QW is increased. For example, the ground state energy shift in a 15 nm GaAs/$Al_{0.4}Ga_{0.6}As$ QW, is in the order of 25 meV at an electric field of 120 kV/cm, while at lower fields of around 30 kV/cm the shift is only around 2 meV [9]. However, for the InAs QDs studied in this work, this effect is negligible since the average height of the QDs is 3.5 nm, the effective mass of electrons is three times smaller than in GaAs, and the maximum field applied is 70 kV/cm.

In asymmetrical structures

One way of obtaining a Stark shift also at low applied fields is to introduce asymmetry in the quantum structure [10, 11]. The asymmetry can be introduced via a potential step in the structure, as shown in figure 2.14. Electrons can then either be bound in the deeper narrow well or in the wide shallow well, which can be represented by an InAs QD and an InGaAs/GaAs QW, respectively. The wave functions associated with the electron states in the QDs are localised in the QD, while the QW wave functions are distributed over the QD as well as the QW. When an electric field is applied, the potential energy in the quantum structure varies linearly with the electric field. The positions of the energy levels then approximately follow the band edge at the centre of the QD and the QD+QW, respectively (figure 2.14). The voltage drop of the energy levels in the QD and the QD+QW, respectively are not equal, see equations (2.33)-(2.36):

$$\Delta E_{+V} = V_0 - qFz_{QD} - \varepsilon_{QD} - (V_0 - eFz_{QW} - \varepsilon_{QW}) \quad (2.33)$$

$$\Delta E_{+V} = \Delta E_0 + qF(z_{QW} - z_{QD}) \quad (2.34)$$

$$\Delta E_{-V} = V_0 + qFz_{QD} - \varepsilon_{QD} - (V_0 + eFz_{QW} - \varepsilon_{QW}) \quad (2.35)$$

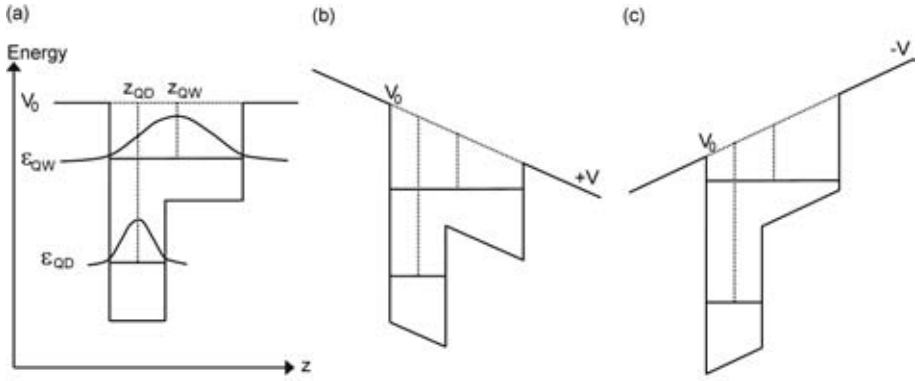

Figure 2.14: Illustration of the bias dependence of energy level separation in an asymmetrical structure. Energy level structures at (a) zero bias (b) positive applied bias (c) negative applied bias.

$$\Delta E_{-V} = \Delta E_0 - qF(z_{QW} - z_{QD}) \tag{2.36}$$

where $\Delta E_0 = \varepsilon_{QW} - \varepsilon_{QD}$ is the energy separation at zero bias. This results in a Stark shift of the energy separation, increasing linearly with the applied field.

2.8.3 Field-induced escape mechanisms

The thermal emission mechanism is governing the escape from QDs or QWs, when no electric field is present. The activation energy needed in the escape process is then gained from the thermal energy, which is why the emission rate is strongly temperature-dependent. The tilting of the band structure, caused by the electric field, increases the number of escape mechanisms available for an electron or a hole trapped in a potential well in the material. In addition to the thermally activated escape, available at zero electric field, there are three further escape routes:

- Poole Frenkel ionization
- Tunneling
- Phonon-assisted tunneling

These escape routes are shown schematically in figure 2.15 and are described in more detail in the following subsections.

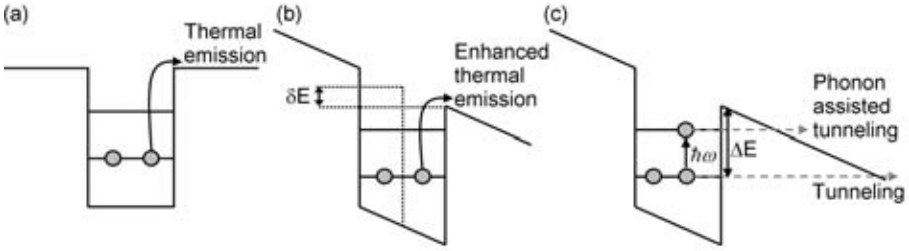

Figure 2.15: Different escape routes from a square well without (a) and with (b, c) an electric field: (a) Thermal emission (b) Enhanced thermal emission due to barrier lowering by δE (Poole-Frenkel effect) (c) Tunneling and phonon-assisted tunneling through a triangular barrier.

Poole Frenkel effect

When the band structure is tilted, a lowering of the barrier surrounding the potential well takes place. Consequently the thermal energy needed for carriers to escape decreases. The associated increase of the emission rate (e_n) can be described by equation (2.37):

$$e_n(F) = e_{n0} e^{\frac{\delta E(F)}{k_B T}} \tag{2.37}$$

where e_{n0} is the emission rate at zero bias and δE is the energy drop of the potential barrier, which varies with the electrical field, F [9, 12, 13]. For a square well potential with a radius r, this energy drop is given by:

$$\delta E(F) = qFr \tag{2.38}$$

Tunneling

The wave functions of electrons (and holes) which are confined inside QWs or QDs are not completely blocked out from the surrounding barrier. Instead, the wave function decreases exponentially in the barrier with a slope determined by the barrier height. If the barrier is thin enough, the amplitude of the wave function will not be zero outside the barrier, which means that there is a certain probability that the electrons escape from bound states in the QD or QW via tunneling through the barrier. At an applied electric field, the shape of the barrier is approximately triangular and the width of the barrier decreases with increasing electric field. Consequently, the transmission probability will increase with increasing electric field. The probability of this event can be approximated by;

$$\tau = exp(-\frac{4}{3}\sqrt{\frac{2m^*}{\hbar^2}}\frac{(\Delta E)^{3/2}}{qF}) \tag{2.39}$$

where m^* corresponds to the effective mass of the charge carrier, $\hbar$ is Planck's constant and ΔE is the height of the barrier with respect to the energy level of the charge carrier.

Phonon-assisted tunneling

The phonon-assisted tunneling is a two step process which combines thermal activation and tunneling. The first step involves thermal excitation to a higher energy level, with assistance of phonons. In a second step tunneling through the triangular barrier occurs. Tunneling from this higher energy level is favourable due to the decreased width of the barrier at this position.

This chapter has given a brief introduction to the subject of semiconductors. For further reading the following references are recommended: [4, 14, 15, 16, 17]

CHAPTER 3

Growth techniques

3.1 Epitaxy

Epitaxy is a controlled way of growing a solid film on a crystalline substrate, in which the atoms of the growing film adjust to the atomic arrangement of the substrate atoms. The two main epitaxial methods used are molecular beam epitaxy (MBE) and metal-organic vapour phase epitaxy (MOVPE) [23]. In MBE, the material to be deposited is evapourated in ultra high vacuum (UHV), where epilayers crystallise when the atoms hit the hot substrate. Since MBE is operated under UHV, simultaneous characterisation of the growing film is possible. This fact makes this method very popular in research environments. However, the growth rate is very slow, which limits the thickness of the film to be grown. MOVPE is a chemical method used to grow semiconducting materials, which does not require as high vacuum as MBE and the growth rate in MOVPE is in general higher. MOVPE is therefore a preferred method for industrial applications.

3.1.1 Metal-organic vapour phase epitaxy

The sources (precursors) used in MOVPE are organo-metals, such as tri-methyl gallium (TMGa) and tri-methyl indium (TMIn), but also pure gases such as arsine (AsH_3) and phosphine (PH_3). The source materials in MOVPE are mainly kept in liquid phase in so-called bubblers, in which the vapour pressure can be regulated by the temperature. A carrier gas (H_2 or N_2) is passed through the bubbler in order to pick up the amount of vapour needed for

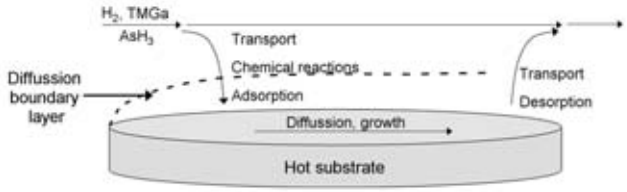

Figure 3.1: Growth process in metal organic vapour phase epitaxy.

growth. The amount of gas picked up can be regulated by the pressure in the bubbler and the mass flow through the bubbler. The desired mixture of precursors is then transported to the reaction chamber by the carrier gas. As the gases approach the hot substrate, the precursor molecules are decomposed and the semiconductor material is deposited from the atomic species. Mass transport occurs by diffusion, through a *diffusion boundary layer* (Fig 3.1). The diffusion is driven by the lower chemical potential at the surface of the substrate. Waste products from the chemical reaction are transported away by the carrier gas.

3.1.2 Molecular beam epitaxy

In MBE, elemental sources are used, which are vapourized in so-called *Knudsen cells*. Knudsen cells are formed in such a way that a collimated beam leaves the entrance of the cell, ensuring a beam of the atoms flows towards the surface of the substrate. The UHV environment allows atoms to reach the surface without collisions. Mechanical shutters in front of each source are used to regulate the beam fluxes. The substrate surface is held at an elevated temperature and when the atomic beams of the constituent elements hit the surface, crystallization of monolayer thick epitaxial layers is enabled.

3.2 Crystal growth

3.2.1 The driving force of growth

During vapour phase growth, two phases coexist; a solid phase which corresponds to the substrate or the already grown epilayer, and the vapour phase, containing the material to be grown. According to the thermodynamics, the material in each phase has a certain energy, called the Gibbs free energy, G. When material moves from one phase to the other, this corresponds to a change in the chemical potential $\mu = \frac{dG}{dn}$, where n is the number of moles of the material. The two phases are in equilibrium, when a transport of atoms from one phase to the other causes no change in the total energy $(\left(\frac{dG_{tot}}{dn}\right)^{vapour} -$

$\left(\frac{dG_{tot}}{dn}\right)^{solid} = 0$). However, this is not the case in the growth chamber. Instead a deviation from the equilibrium is established, where a reduction of the total energy is achieved when the atoms go from the vapour phase to the solid phase. In other words, the chemical potential of the solid phase is lower than the chemical potential of the vapour phase.

A necessary condition for phase transitions to occur, according to thermodynamical driving forces, is sufficient energy, needed to overcome possible activation energies. Sufficient energy is likely to be provided at high temperatures. However, at low temperatures, kinetics might govern the growth process, consisting of chemical, thermal and mass transfer processes.

3.2.2 Crystallisation

Atoms impinging on the substrate can lower their energy by making bonds to the atoms in the crystal. Depending on the surrounding of the adsorbed atom (adatom), the energy gain will differ. The adatoms therefore move on the surface until a site of lowest energy is found. Preferred sites of incorporation are steps and kinks, since the energy gain is high at these sites, while the energy gain is low for making bonds to flat terraces. Steps normally occur naturally on monocrystalline substrates due to slight misorientation from the lattice plane, which gives rise to monolayer steps. If no such steps exist, nucleation is required for growth to occur, i. e. formation of small clusters of atoms, which act as starting points for growth.

3.2.3 Growth modes

There are five distinguishable growth modes of crystal growth:

- Frank van der Merwe (layer growth)
- Volmer-Weber (island growth)
- Stranski-Krastanow (layer + island growth)
- step flow mode
- columnar growth

Which type of growth mode prevails depends on the lattice misfit between the substrate and the material to be grown on the substrate (the *epilayer*) together with the growth conditions (temperature, flux etc). In order to distinguish between the first three growth modes, the relationship between the interface energy between the substrate and the epilayer, $\gamma_{s/e}$, and the surface energy of the substrate, $\gamma_{s/v}$, and the epilayer, $\gamma_{e/v}$, respectively, can be used. If the sum of the interface energies between epilayer/vapour and substrate/epilayer

is less than the interface energy between substrate and vapour (Eq. 3.1), it is energetically favourable for the epitaxial layer to cover the substrate.

$$\gamma_{e/v} + \gamma_{s/e} < \gamma_{s/v} \tag{3.1}$$

This condition (Eq. 3.1) can be fulfilled when the substrate and the epilayer are lattice matched, as well as for a small lattice mismatch between substrate and epilayer ($< 2\%$). On the other hand, for a large lattice mismatch between the substrate and the epilayer ($> 10\%$), the sum of the epilayer/vapour and substrate/epilayer interface energies is larger than the substrate/vapour energy (Eq. 3.2).

$$\gamma_{e/v} + \gamma_{s/e} > \gamma_{s/v} \tag{3.2}$$

In this case, it is more favourable for the epilayer to form 3D islands, instead of covering the surface of the substrate. When there is an intermediate lattice mismatch between the substrate and the epilayer ($\sim 2 - 10\%$), condition 3.1 is fulfilled for the first monolayers of the growth, but as the strain energy in the epilayer increases with thickness, a critical thickness is reached, when the energy conditions is fullfills equation 3.2 instead of equation 3.1. This two step process is referred to as the Stranski-Krastanow growth mode, which is the growth mode used for self-assembly of quantum dots. More details about the quantum dot growth is given in section 3.2.4

The last two growth modes to be described are the step flow growth and the columnar growth. Step flow growth occurs when the mobility of atoms on the surface is high enough, realised by high substrate temperatures. In this growth mode, atoms can be incorporated at step-edges immediately and the step propagates forward in a uniform manner, resulting in high quality epitaxial layers. Columnar growth requires opposite growth conditions compared to the step flow growth, i. e. low mobility of atoms on the surface. As indicated by the name, separate columns grow without merging with each other, as would be the case for Volmer-Weber and Stranski-Krastanow growth modes, if the growth was continued after the island formation.

3.2.4 Quantum dot growth

Quantum dots are grown using self assembly in the Stranski-Krastanow growth mode [24, 25]. The growth is an energy driven process, where the system minimizes energy through transition from a highly strained layer to islands. There are four different phases which quantum dots undergo during this layer to island transition:

- 2D layer-by-layer growth
- Nucleation
- Island growth
- Ripening

During the layer-by-layer growth, the strain energy increases with the deposited volume (Region A, Fig: 3.2). At first, the layer growth is stable, but when a certain thickness (t_{cw}) of the wetting layer is reached, the growth enters a metastable phase and as soon as the energy needed to undergo the transition from a layer to islands is reached, the nucleation process starts (Point X, Fig: 3.2). During nucleation, material from the wetting layer as well as from additional deposited material is consumed. The time span of the nucleation phase is quite short, since the excess energy in the wetting layer drops with the consumption of the wetting layer material (Region B, Fig: 3.2). When the total energy is less than the nucleation energy, the nucleation phase stops and thereby the density of dots is defined (Point Y, Fig: 3.2). During and after the nucleation phase, material diffuses toward the islands due to the lower potential energy at the dots, since the islands are less strained than the wetting layer. This activity represents the island growth phase. During the ripening phase, the material which is still mobile will diffuse toward the islands and some redistribution of material between islands takes place (Region C, Fig: 3.2).

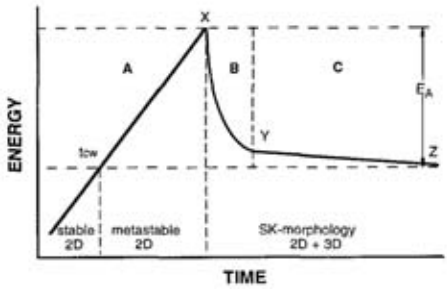

Figure 3.2: The different growth phases during quantum dot growth [24].

CHAPTER 4

Infrared detectors

4.1 Infrared radiation

Infrared (IR) radiation covers the wavelength region in the electromagnetic spectrum between visible light and microwaves, i.e. between 770 nm and 1 mm. IR radiation is emitted by all bodies as thermal radiation but depending on the body temperature, the emission spectrum exhibits different spectral distributions. Hot objects, exceeding temperatures of 1000 K, are radiating in the visible wavelength region, which enables estimation of their temperatures by the colour of the radiation, while cooler objects, such as human bodies, are radiating in the infrared region. This dependence of the spectral radiation with temperature is described by Planck's radiation law:

$$M(\lambda) = \frac{2\pi hc^2}{\lambda^5(exp(\frac{ch}{\lambda kT}) - 1)} \quad \left[\frac{W}{m^2 \mu m}\right] \tag{4.1}$$

where λ is the wavelength, T is the temperature and the constants c, h and k correspond to the speed of light, Planck's constant and Boltzmann's constant, respectively. The temperature dependence of Planck's radiation law is visualised in Fig. 4.1 for temperatures ranging from 200 to 6000 K. However, part of the emitted radiation is absorbed in the atmosphere by water vapour and carbon dioxide and the actual radiation observed in the IR wavelength region is shown in figure 4.2. Due to the transmission properties of the atmosphere, the IR wavelength region can be subdivided into four different regions:

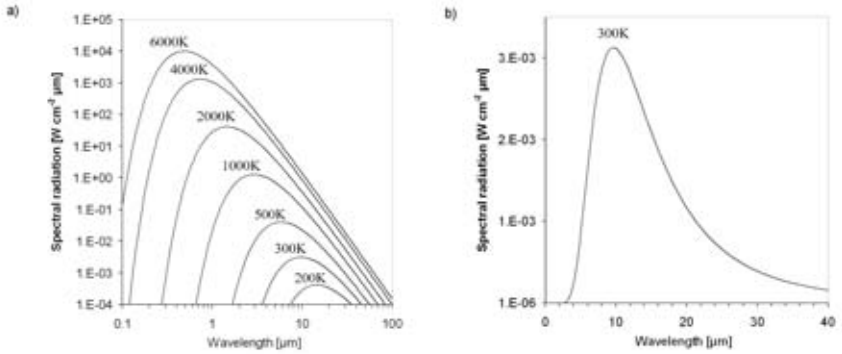

Figure 4.1: Spectral radiance according to Planck's radiation law (a) at temperatures ranging form 200 K to 6000 K (b) at 300 K.

- Near infrared (NIR, 770nm - 3μm)
- Medium wavelength infrared (MWIR, 3 - 5 μm)
- Long wavelength infrared (LWIR, 8 - 14 μm)
- Far infrared (FIR, 16 μm - 1 mm)

The MWIR and LWIR transmission windows are the ones used for thermal imaging, since these have the strongest correlation with the emission wavelengths of the objects in our surrounding (Fig. 4.1 b). NIR is an important transmission window for free-space optical communication and FIR is used in terahertz technology, for example. The transmission is not fixed, but depends strongly on the temperature and humidity in a certain climate. In arctic climates, the transmission is high in the LWIR region but suppressed in the MWIR region, while in tropical climates the opposite is true for the LWIR and MWIR regions [26].

4.2 Detector technologies

The total radiation emitted from a black body with a temperature T, can be found by integration of Planck's radiation law over all wavelengths. The relation subsequently achieved is Stefan-Boltzmann's law, given in equation 4.2, where σ is Stefan-Boltzmann's constant.

$$W_{bb} = \sigma T^4 \quad \left[\frac{W}{m^2}\right] \tag{4.2}$$

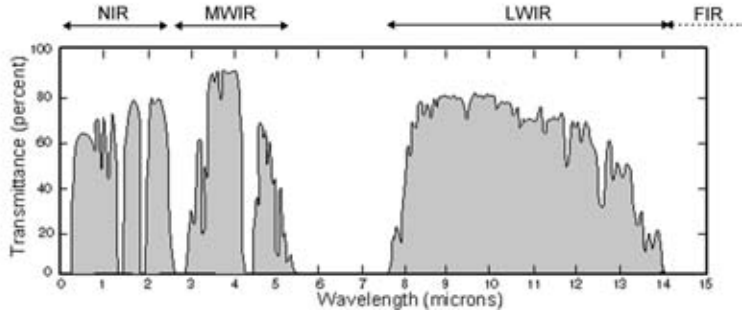

Figure 4.2: Transmission of infrared radiation through the atmosphere at distance of 1852 m, a temperature of 15.5°C and a humidity of 70 % at sea level.

The knowledge of the relationship between the temperature and the emitted power, enables determination of the temperature of a black body by measurement of the corresponding thermal radiation. For non-black bodies, i. e. bodies which do not absorb (and emit) all incident radiation, the emitted power for a certain temperature is lower than the corresponding radiation from a black body. The emitted power is lowered by a wavelength dependent factor ε, called the emissivity. Consequently, knowledge of the emissivity is also required in order to enable determination of the temperature of an object.

Two main detector technologies are used to measure the thermal radiation - *thermal detectors* and *photon detectors*. Thermal detectors are based on a two step process, where first the detector material is heated by the incident radiation and then some temperature dependent physical property, such as the resistivity of the material, is measured. The advantage of thermal detectors is that they can be operated at room temperature, but as a drawback they have a rather slow response and the sensitivity is normally lower than for a photon detector. In photon detectors, the incident photons cause excitation of charge carriers, which either gives rise to a change in an electrical current or voltage in the device. The advantages of these detectors are that they are highly sensitive and have a fast response, but they need to be cooled to cryogenic temperatures in order to reduce the so-called dark current (see section 4.3.3).

4.2.1 Photon-detecting materials

Photons incident on a detector can be absorbed by electrons in the detecting material, given that the photon energy exceeds the energy needed to excite the electrons to a higher energy level. In a bulk material, the transition of the electron can either be from the valence band to the conduction band (intrinsic detection) or from a dopant level to the conduction or valence band (extrinsic detection), see figure 4.3. In a second step, the electron can be observed through

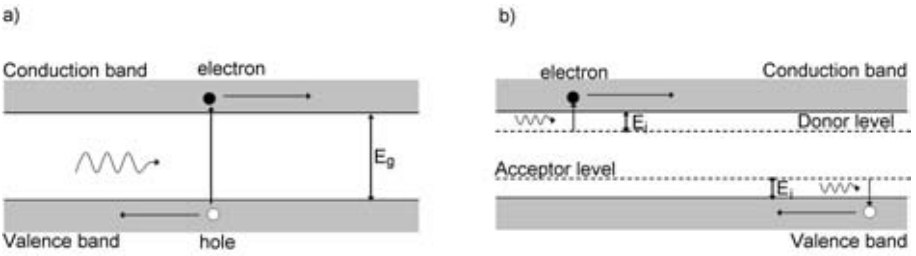

Figure 4.3: Detection principle of a) intrinsic b) extrinsic detectors.

Table 4.1: Bandgap energies and dopant levels of some bulk materials [27].

	Band gap		Dopant level		Detection type
	[eV]	[μm]	[eV]	[μm]	
InSb	0.23	5.4			
$Hg_{0.7}Cd_{0.3}Te$	0.25	5			intrinsic
$Pb_{0.2}Sn_{0.8}Te$	0.1	12			intrinsic
$Hg_{0.8}Cd_{0.2}Te$	0.1	12			intrinsic
Ge:Au			0.15	8.3	extrinsic
Ge:Hg			0.09	14	extrinsic
Si:In			0.155	8	extrinsic
Si:Ga			0.072	17	extrinsic

its contribution to an electrical current or voltage. The band gap energies and dopant levels of some materials, which can be used for infrared detection are given in table 4.1.

The number of materials with either intrinsic bandgaps or extrinsic dopant levels in the MWIR or LWIR region is limited. However, by using quantum structures, new possibilities to design the band structure of a material arise, enabling detection in these wavelength regions. One common type of detector which has been enabled by the use of quantum wells (QWs) or quantum dots (QDs) is the intersubband detector. The detection principle in these detectors is based on intersubband transitions between different energy bands/levels within the conduction band (or valence band).

4.2.2 Photon detectors

Interband detectors

In interband (intrinsic) detectors, the detection wavelength is determined by the band gap of the material and can be realized by e.g. InSb, $Pb_{0.2}Sn_{0.8}Te$ or $Hg_{0.8}Cd_{0.2}Te$ for MWIR or LWIR detection. The most common device type

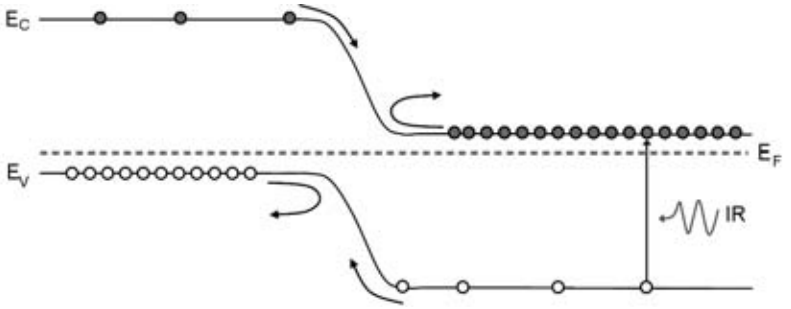

Figure 4.4: Detection principle of a photovoltaic detector realized by a p-n junction.

used for interband IR-detectors is the photovoltaic pn-diode. A pn-diode is formed by combining a p-doped and a n-doped region in the material. Since the Fermi levels in the two regions are different, band bending occurs through redistribution of free charge carriers. This results in a depletion region and a built-in electric field at the interface between the two regions (Fig. 4.4). In the photodiode, electron-hole pairs are generated by the incident radiation and the minority carriers (holes in the n-type material and electrons in the p-type material), which diffuse towards the depletion region are accelerated by the built-in field and collected, while the majority carriers are reflected by the barrier. A photovoltaic effect is thus obtained without external bias, since photo-excited carriers accumulate on their respective low energy side of the p-n junction. However, the read-out is often operated under reverse bias in a photoconductive mode measuring the photocurrent through an external load resistor.

Intersubband detectors

Intersubband detectors are realized by quantum structures, where the charge carriers are confined in at least one direction, enabling quantisation of the energy levels of the carrier (Fig. 4.5). The design of an intersubband detector is based on the fact that the energy difference between the electron (or hole) ground state and an excited state within the conduction band (valence band) corresponds to the desired detection wavelength. Electrons (holes) populating the ground state can thus absorb photons with that specific energy and be excited to higher energy states. The excited electrons (holes) can in a subsequent step escape from this energy state and contribute to the photocurrent.

Quantum well infrared photodetectors (QWIPs) is one of the main detector types used for IR imaging. The detection wavelength of the device can be tailored by adjusting the width and composition of the QWs, which determines the energy separation between the quantised energy levels. The most common material system used for quantum well infrared photodetectors

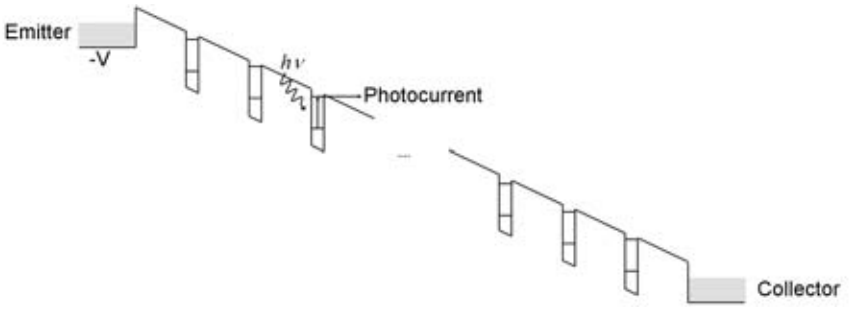

Figure 4.5: Detection principle of an intersubband detector.

(QWIPs) is the GaAs/AlGaAs multiple QW, in which intersubband transitions occur in the conduction band. QWIPs have also been realised for the SiGe/Si material system, based on intersubband transitions in the valence band. The thin QW layers are grown with epitaxial techniques and high uniformity of the detector arrays can thereby be achieved.

The **quantum dot infrared photodetector** (QDIP) is a further development of a QWIP, in which the QWs are substituted by quantum dots (QDs, see section 2.5.3) as the active material for IR absorption. As in QWIPs, the detection wavelength can be determined by the size and composition of the QDs. However, the fact that the energy levels in the QDs are fully quantised gives additional advantages. The discretised energy levels in QDs act to suppress the dark current in the detectors, which enables higher operating temperatures. Furthermore, QDs can absorb light at all angles of incidence, while QWs only can absorb light with the electric field polarised in the quantisation direction of the QW. This simplifies the fabrication process of QDIP devices, since gratings used to change the polarisation of the incoming radiation, in order to enable absorption, are no longer necessary. QDIPs can be realized both in MWIR as well as in the LWIR region.

A more recent and advanced technique to realize detection in the LWIR region is by embedding QDs in a QW in so called **quantum dots-in-a-well infrared photodetectors** (DWELL IPs), where the detection is governed by transitions between QD and QW states (Fig. 4.6). This method offers additional degrees of freedom to tailor the detection wavelength of the device: partly by varying the QD energy levels (by varying size and composition) and partly by adjusting the width and composition of the QW [28, 29, 30, 31]. For example, by using InAs QDs embedded in an $In_{0.15}Ga_{0.85}As$ QW, the peak detection wavelength can be shifted from 7 to 11 μm by changing the width of the QW from 7 to 12 nm [29]. Another way to tune the detection wavelength, enabled in DWELL IPs, is to employ asymmetrical positioning of the QD layer inside the QW (Figs. 4.7a and 4.8a). The energy level separation

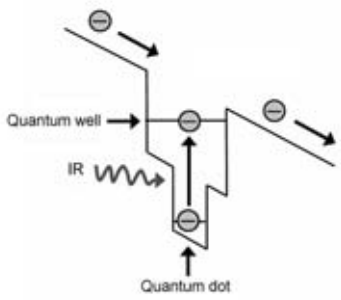

Figure 4.6: Detection principle of a quantum dots-in-a-well infrared photodetector.

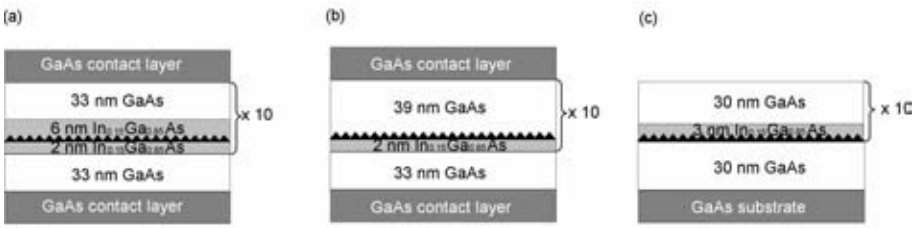

Figure 4.7: Three different quantum dots-in-a-well structures with different symmetries of the InAs QD layer with respect to the $In_{0.15}Ga_{0.85}As$ QW: (a) Asymmetrically positioned inside an 8 nm wide QW, (b) Positioned on top of a 2nm wide QW (dots-on-a-well), (c) Symmetrically positioned inside a 3 nm wide QW.

between the QD and QW states accordingly varies with the applied bias, which results in a bias tunable detection wavelength (see section 2.8.2) [32, 33]. In paper IV in this work, tuning of the detection wavelength from 8.4 to 10.3 μm was demonstrated, by varying the applied bias. This enables IR-detection in different wavelength bands within the same pixel, which is favourable for dual colour detection.

Dual colour detection can also be achieved in DWELL IPs by employing several intersubband transitions, which alternatingly dominate the photocurrent. The possibility to toogle the detection wavelength between the MWIR and LWIR detection regions has been demonstrated for DWELL detectors, by using bound-to-bound (from QD to QW energy levels) and bound-to-continuum (from QD energy levels to GaAs matrix) intersubband transitions, respectively [34]. This feature is also enabled by using a dots-*on*-a-well IP (Fig. 4.7b), as demonstrated in paper IV.

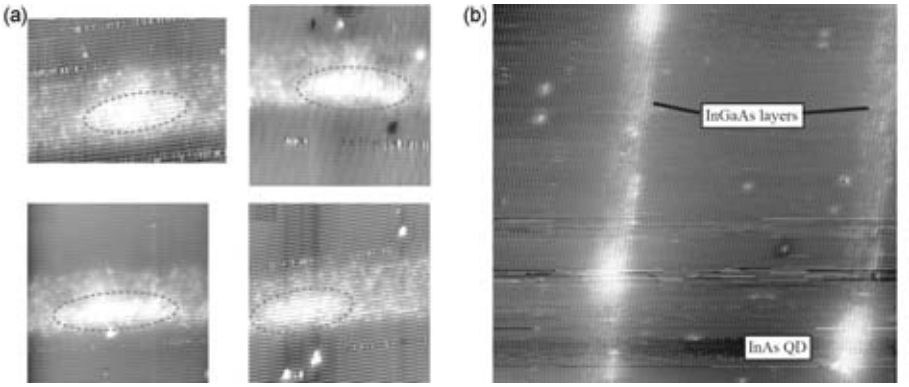

Figure 4.8: Cross-section scanning tunneling micrographs (XSTM) of two different quantum dots-in-a-well structures: (a) asymmetrically positioned inside an 8 nm wide $In_{0.15}Ga_{0.85}As$ QW (corresponding to Fig. 4.7a), (b) symmetrically positioned inside a 3 nm wide $In_{0.15}Ga_{0.85}As$ QW (corresponding to Fig. 4.7c) [35].

4.3 Figures of merit of infrared detectors

To enable comparison of different IR detectors, there are a number of figures of merit, which are used. For single pixel devices, responsivity, dark current and detectivity (D^*) are commonly used measures. For detector arrays, the noise equivalent temperature difference (NETD) is more commonly used.

4.3.1 Responsivity

The responsivity of a detector is a measure of the response of the detector, when it is irradiated with a certain power of radiation (measured in A/W or V/W). There are two parameters, which are of outmost importance for this measure; the quantum efficiency and the internal gain in the detector, which are described in the following sections.

Quantum efficiency

Light which travels through a material attenuates as $I_0 e^{-\alpha l}$, where I_0 is the initial intensity of the light, α is the absorption coefficient and l is the thickness of the material. Consequently the ratio between the absorbed light and the incident light is given by;

$$\eta_a = \frac{I_0 - I_0 e^{-\alpha l}}{I_0} = 1 - e^{-\alpha l} \tag{4.3}$$

which is the absorption quantum efficiency. In quantum structures, the absorption quantum efficiency is related to the quantum efficiency (number of

photogenerated carriers for each incident photon) via the transmission factor γ, if tunneling through the barrier is part of the escape process (see section 2.8.3). This provides us with a relation between the absorption coefficient and the quantum efficiency ($\eta = \gamma\eta_a$), which is useful when comparing measurement results with theoretically calculated values of the quantum efficiency and the absorption coefficient, respectively.

Photoconductive gain

Electrons (or holes), which have been excited by absorption of photons, can contribute to the photocurrent in a detector, as illustrated in the figures 4.4 and 4.5. However, there is a certain probability, that the excited charge carriers do not reach the contacts. In interband detectors, electron-hole recombination might occur during the diffussion process and in intersubband detectors the charge carriers might be recaptured by other dots/wells on the way to the collector contact (Fig. 4.9). Furthermore, in intersubband detectors, there is injection of electrons from the emitter contact, added in order to maintain an electron population in the dots/wells. These effects are taken into account in the photoconductive gain, which is the number of charge carriers flowing in an external circuit for each absorbed photon. The gain, g, is given by the ratio between the free carrier lifetime τ and the transit time between the electrodes τ_t ($g = \frac{\tau}{\tau_t}$). In a photodiode, the gain is equal to 1, while in the different intersubband detectors g is typically smaller (for QWIPs) or larger (for QDIPs) than 1. For example, the gain in a GaAs/AlGaAs QWIP is bias-dependent with a saturation value of approximately 0.3 [38]. This can be compared to QDIPs and DWELL IPs, for which gain values around 10 and 3, respectively, have been reported [39, 43].

The explanation of the different gain values in QDIPs and QWIPs is twofold. First of all, the QDs do not cover the whole surface, which results in a decreased capture probability in the QD layers compared to in the QW layers. A second contribution to the higher gain values for QD based detectors is the relaxation process, which is less efficient for QDs than for QWs. Relaxation of captured charge carriers mainly occurs via intermediate energy levels under emission of longitudinal optical (LO) phonons (which have energies of 29 meV in InAs and 36.6 meV in GaAs) [14, 37]. In QWs, this process is relatively efficient since there is a continuous band of energy levels, which can be used as intermediate levels for relaxation. In QDs, there is only a discrete number of energy levels, which can be used for relaxation. If the energy level separation in the QDs does not match the LO-phonon energy, the relaxation process will be slowed down, since simultaneous emission of acoustical phonons is required (phonon bottleneck effect). The probability that the charge carriers will be reemitted during the relaxation process is then increased, which will decrease the total amount of recaptured charge carriers.

As a consequence of the increased gain, the responsivity should be higher

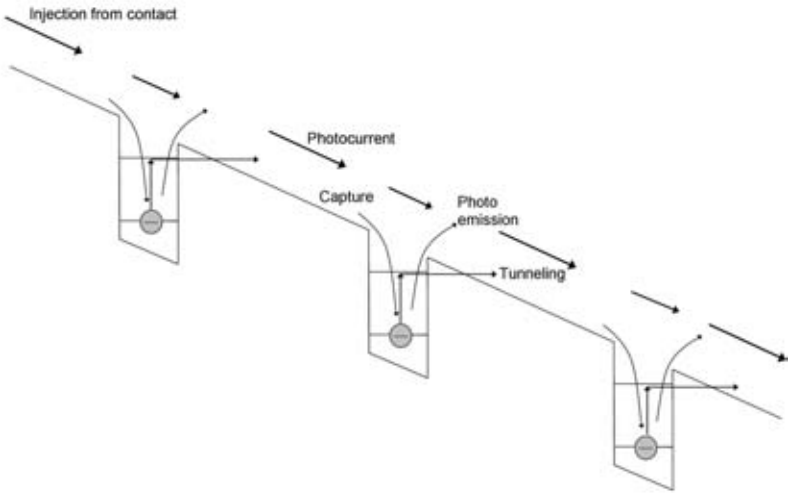

Figure 4.9: Schematic picture of the contributions to the photocurrent.

in a QD based detector, since the responsivity is proportional to the gain (see equation 4.5).

Photocurrent

The photocurrent is the part of the current measured in a detector, which is caused by an incident photon flux (Φ $[\frac{Photons}{cm^2 s}]$). The photocurrent is given by;

$$I_{pc} = qA_{det}\Phi\eta g \qquad [A] \tag{4.4}$$

where A_{det} is the area of the detector, η is the *quantum efficiency* and g is the *internal gain*.

However, since the photon flux and the area of the device is related to the specific measurement setup, the photocurrent is not a good measure for detector comparison. A better measure is the responsivity, which is a normalised (with respect to the area) ratio between the photocurrent and the optical intensity generating the signal. An expression for the current responsivity (R_I) is given by;

$$R_I = \frac{q\frac{P}{\frac{hc}{\lambda}}A_{det}\eta g}{A_{det}P} = \frac{q\lambda}{hc}\eta g \qquad [A/W] \tag{4.5}$$

Instead of the photon flux (in eq. 4.4), the power density P $[W/cm^2]$ is used. The relation between the photon flux and the power density is: $\Phi = P/\frac{hc}{\lambda}$, where $\frac{hc}{\lambda}$ is the energy of a photon with wavelength λ. The magnitude of the responsivity depends on the gain and the quantum efficiency, which means that this measure of the performance of the detector, depends on both high absorption and a long lifetime of the excited charge carriers.

4.3.2 Dark current

Dark current is the current measured in a detector, when no photo-excitation occurs. In photodiodes, there are three different contributions to the dark current, which are alternatingly dominant at different temperatures: diffusion current, generation-recombination current and tunneling. In addition, surface leakage currents might play an important role, if the surface is not properly passivated.

Dark current in intersubband detectors is generated by three different physical mechanisms: thermal emission, tunneling and phonon assisted tunneling as described in section 2.8.3. Thermal emission, i.e. when electrons are thermally excited out of the QW to the continuum states, has been shown to be the main source of dark current in QWIPs [44]. It can be assumed that thermal emission also plays an important role for QDIPs and DWELL IPs. The differences between the structures, which have an effect on the dark current, will now be described.

Dark current in quantum well infrared photodetectors

In a QW, there is a continuous energy band above each quantised energy level, due to the plane-wave character of the electrons in the plane of the QW (Fig 4.10a). As the temperature increases, electrons occupy higher energy levels in the bands, according to the Fermi-Dirac distribution $(1 + e^{(\varepsilon_1 - \varepsilon_f)/k_B T})^{-1}$, which alleviates thermal emission. Consequently, the dark current increases rapidly as the temperature increases. The dark current in a QWIP can be reduced by cooling of the detector, thereby allowing electrons to occupy just the lowest energy levels in the structure.

Dark current in quantum dot based infrared photodetectors

In a quantum dot the electrons are trapped in all three dimensions, which results in discretised energy levels, as has been depicted in figures 4.10b and 4.10c. The electrons in the ground state of the quantum dot then need a higher external energy contribution as compared to electrons in a quantum well in order to escape from the dot. This results in a reduction of the dark current for **QDIPs** as well as for **quantum dots-in-a-well structures**, since the electrons are trapped in the QD ground states in both cases.

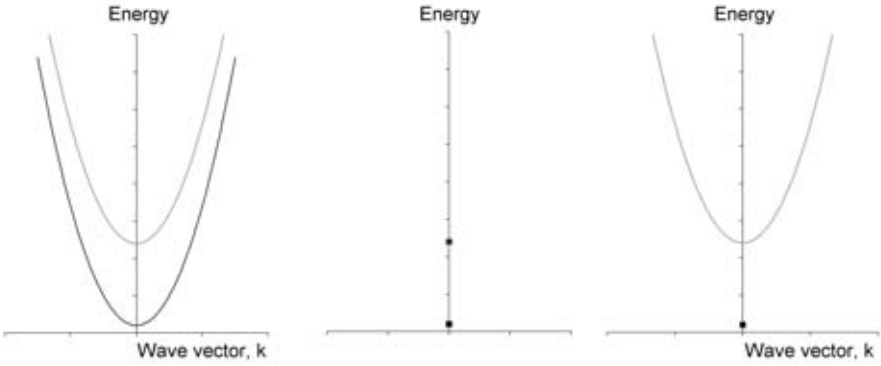

Figure 4.10: Energy dispersion for electrons in a (a) quantum well (b) quantum dot (c) quantum dots-in-a-well. k corresponds to the wave vector in the plane of the QW (see equation 2.11) and is relevant only for the QWs.

4.3.3 Noise

In photon detectors, there are several material related sources of noise, with different degree of importance depending on the detector type [27]:

- Johnson noise,
  which exists in any resistive material and is due to random motion of charge carriers. Johnson noise differs from the other three noise sources in that it is present also without bias.

- Generation-recombination noise,
  which is caused by fluctuations in the generation and recombination of free charge carriers. In extrinsic detectors, generation and recombination mainly occur via the dopant level used for detection, while in intrinsic detectors, fluctuations in the interband generation and recombination are cause this noise.

- Shot noise,
  which is present in photodiodes operated under bias and is caused by fluctuations in the arrival rate of carriers accelerated by the built-in electric field.

- Flicker noise (1/f-noise),
  which gives a significant contribution at low frequencies, but is of less importance at higher frequencies as it decreases as 1/f. The flicker noise is related to traps and boundaries in a material and can be significantly reduced in high quality monocrystalline materials.

The common limitation of the detectors is the background photon fluctuation noise, related to the background photon flux, which the detectors are exposed to.

Background photon fluctuation noise

The detector is not only exposed to the radiation from the object to be detected, but also to radiation from the background. The background photon flux (Φ_B) includes the flux collected from the optics as well as the radiation emitted from the housing of the detector. The number of background photons absorbed by the detector fluctuates in time and cause background noise in the detector (Eq. 4.6):

$$i_{n,B}^2 = 4e^2 g^2 \eta \Phi_B \Delta f \tag{4.6}$$

There are many parameters, which influence the magnitude of the background flux incident on the detector. The temperature of the emitting background is one important parameter and also the field of view, which is the solid angle to the detector monitoring background flux. The field of view is limited by the lens diameter, given that the detector housing is cooled or if the radiation from the housing is supressed by other means.

When comparing different detectors, the background temperature and the f-number ($f\#$) are normally given. The f-number is related to the solid angle (2θ) as:

$$f\# = \frac{1}{2sin\theta} \tag{4.7}$$

$f\#$ can be approximated by $\frac{L}{D}$, where L is the distance between the lens and the detector element and D is the diameter of the lens (Fig. 4.11). This shows the importance of the size of the optics for the background flux.

4.3.4 Detectivity

In order to evaluate the performance of a detector, the combined effect of the responsivity and the thermal noise should be considered. The most common measure used is D^*;

$$D^* = \frac{R_I}{\frac{i_{noise}}{\sqrt{A\Delta f}}} = \frac{\frac{qg\eta}{h\nu}}{\sqrt{\frac{i_{n,dark}^2}{A\Delta f} + \frac{i_{n,B}^2}{A\Delta f}}} \qquad [cmHz^{1/2}/W] \tag{4.8}$$

where R_I is the responsivity, Δf is noise bandwidth, A is the detector area, $i_{n,dark}$ is the dark current noise and $i_{n,B}$ is the detector noise caused by the background radiation (equation 4.6). The unit of D^*: $cmHz^{1/2}/W$ is also

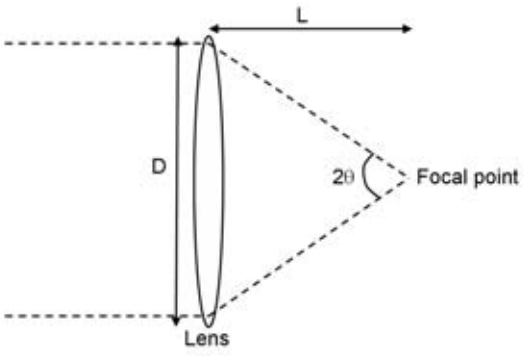

Figure 4.11: Illustration of the lens and the focal plane array, with the angle α, defining the f-number of the measurement setup.

called *Jones*. Another measure, which directly relates the responsivity and the noise current is the detectivity, ($D = R_I/i_{noise}$). However, this relation is less frequently used in the literature, although the name (detectivity) is sometimes used for D*.

Normally the operating temperature of the detector is decreased until the background noise exceeds the dark current noise, resulting in a background limited infrared photodetector (BLIP). The corresponding temperature, when the dark current noise equals the background noise is the BLIP-temperature, T_{BLIP}. For $T \leq T_{BLIP}$:

$$D^*_{BLIP} = \frac{\frac{qg\eta}{h\nu}}{\sqrt{4e^2g^2\eta\Phi_B}} = \frac{1}{h\nu}\sqrt{\frac{\eta}{4\Phi_B}} \tag{4.9}$$

As can be seen in equation (4.9), the ultimate D^* of the detector at the BLIP temperature, i. e. D^*_{BLIP}, is independent of the gain and dark current. Nevertheless, the BLIP temperature is highly dependent on the dark current. Consequently, in order to increase D^*_{BLIP}, the most important parameter to optimize is the quantum efficiency. In order to decrease the BLIP temperature, the dark current should be decreased.

Assuming that the background fluctuation noise is negligible compared to the dark current, the influence of the dark current alone on the detector performance can be studied. This thermal detectivity (i.e. $D^*_{thermal}$) is given by:

$$D^*_{thermal} = \frac{R_I}{\frac{i_{n,dark}}{\sqrt{A\Delta f}}} \qquad [cmHz^{1/2}/W] \tag{4.10}$$

In order to achieve the performance given by the thermal detectivity, the size

Table 4.2: Theoretically predicted thermal D^*-values for MWIR and LWIR detection for different detector materials and theoretical BLIP-temperatures for different detectors with a detection wavelength cut-off (λ_c) at 10 μm. The conditions for these BLIP-temperatures correspond to f/2-optics and a background temperature of 300K [40]. The value of the quantum efficiency used for HgCdTe refers to the quantum efficiency without antireflection coating. An experimentally reported value of the quantum efficiency is used for the QDIP in this table.

	Quantum efficiency	BLIP temperature ($\lambda_c = 10\mu m$)	$D^*_{Thermal}$ @ 5 μm, 120 K [Jones]	$D^*_{Thermal}$ @ 10 μm, 60 K [Jones]
N-HgCdTe	67 %	120 K	$1 \cdot 10^{14}$	$7 \cdot 10^{13}$
QDIP	2 %	120 K	$4 \cdot 10^{12}$	$2 \cdot 10^{12}$
QWIP	33 %	65 K	$1 \cdot 10^{11}$	$2 \cdot 10^{11}$
Extrinsic	35 %	52 K	$8 \cdot 10^{9}$	$1.5 \cdot 10^{10}$

of the optics needs to be chosen in such a way that the background flux indeed is lower than the dark current.

4.4 Comparison between different detector technologies

In order to judge the potentially achievable performance of different detector materials, there are two parameters which are of utmost importance; the absorption quantum efficiency and the dark current. Knowing these parameters, D^*_{BLIP} and the BLIP-temperature can be determined for different background fluxes.

A theoretical comparison between different detector materials have been made by Martiniuk and Rogalski [40] (see table 4.2). This theoretical comparsion shows that the photodiode HgCdTe has outstanding detectivities in MWIR as well as in LWIR among the photon detectors. However, in reality HgCdTe is a mature material only for MWIR detection. In LWIR, HgCdTe detectors suffer from uniformity and yield problems, which make the detectors expensive to fabricate, especially for large arrays. This makes QWIPs competitive to HgCdTe detectors in the LWIR region, although the detectivity of HgCdTe detectors is much higher than for QWIPs.

The extrinsic detectors seem promising due to relatively high quantum efficiencies. However, they are limited by their low BLIP temperatures, which is a result of high generation-recombination noise in these detectors.

For the QDIPs, it is assumed that the QDs have only two bound energy levels with energy separations corresponding to the desired detection energy. With this arrangement of the energy levels in the QDIP, it is shown that the

BLIP temperatures of QDIPs and HgCdTe detectors for LWIR are equal, while the BLIP temperature of the QWIP is significantly lower. This difference between the QWIP and the QDIP is caused by the reduction of the dark current in QDIPs, discussed in section 4.3.3. However, in order to achieve the predicted performance of the QDIP, the QDs should be small enough to hold at most two energy levels, with an energy separation corresponding to the energy to be detected as modelled. This is very rare for QDs grown in the Stranski-Krastanow growth mode. More commonly, InGaAs-based QDs have electron energy level separations in the order of 30-60 meV, which increases the possibility for thermal excitation to intermediate energy levels, from which thermal emission can occur more easily. This is the reason why QDIPs have not yet proved this superior performance.

Since the DWELL IPs were not part of the theoretical comparison above, an experimental comparison between a DWELL IP and a commercially available GaAs/$Al_{0.3}Ga_{0.7}As$ QWIP (both with a peak detection wavelength at 8.5 μm) was performed (Table 4.3). The parameters compared are the integrated responsivity, the dark current and in addition, the ratio between these two parameters. The DWELL IP corresponds to the component studied in paper III in this study. As can be seen in the comparison, the responsivity values of this DWELL IP are significantly lower than for the optimised QWIP detector. This is partly due to the fact that the QDs are undoped and that the DWELL IP does not include an optical cavity. Nevertheless, due to the low dark current in the DWELL IP, it is still competitive to the QWIP. In fact, when comparing the ratio between responsivity and dark current for applied biases on the DWELL IP up to 2 V, this ratio is higher for DWELL IPs than for QWIPs at corresponding temperatures. At an applied bias of 2.5 V on the DWELL IP, the ratios are comparable to those of the QWIP. Although the DWELL IPs in this comparison are far from optimised, this shows that these detectors have a great potential to compete with QWIP detectors.

Table 4.3: Comparison of dark current and responsivity values of a DWELL IP and a QWIP. The integrated responsivity values were achieved by integration of the responsivity curves in an interval from 7 to 12 μm. Operating temperature of QWIPs is 65 K.

	Temp. [K]	Integrated responsivity [mA/W]	Dark current [$\times 10^{-5}$ A/cm^2]	Integrated responsivity / dark current [$\times 10^4$ $W^{-1}cm^2$]
QWIP	60	512	0.13	39
-1.5 V	65	522	0.8	6.5
	70	530	4.1	1.3
	75	522	17.4	0.3
DWELL	60	0.6	8.5×10^{-7}	7060
IP	70	0.32	3.2×10^{-5}	100
1.5 V	77	0.32	4.8×10^{-4}	6.3
DWELL	60	2.8	5.8×10^{-5}	483
IP	70	2.6	4.4×10^{-3}	5.9
2 V	77	4	4.8×10^{-2}	0.8
DWELL	60	9.5	3.2×10^{-3}	30
IP	70	11	0.12	0.9
2.5 V	77	16	0.96	0.17
DWELL	60	16	0.3	0.5
IP	70	24	3.8	0.04
3 V	77	40	17.3	0.02

CHAPTER 5

Experimental methods

5.1 Photoluminescence

Photoluminescence (PL) measurements are used to detect the radiation associated with the recombination of electrons and holes. In PL measurements, the sample is excited by an external light source (usually a laser) with photon energies larger than the bandgap of the sample. Electrons are excited from the valence band to the conduction band by absorption of the photons. The majority of the electrons and holes relax to the lowest energy position before they recombine and emit radiation with energies corresponding approximately to the bandgap energy (Fig. 5.1a)).

The most common way to analyze the luminescence, is to use a monochromator, which disperses the luminescence with a diffractive grating, allowing a limited wavelength interval to enter the detector situated at the exit of the monochromator. The wavelength resolution is set by a slit at the exit of the monochromator.

5.2 Photoluminescence excitation

Luminescence caused by the recombination of electrons and holes in excited states are more difficult to detect than the ground state luminescence, due to the fast relaxation of electrons and holes to the ground state, particularly at low temperatures. A very useful technique to circumvent this difficulty is to use photoluminescence excitation (PLE) spectroscopy. The detection wavelength

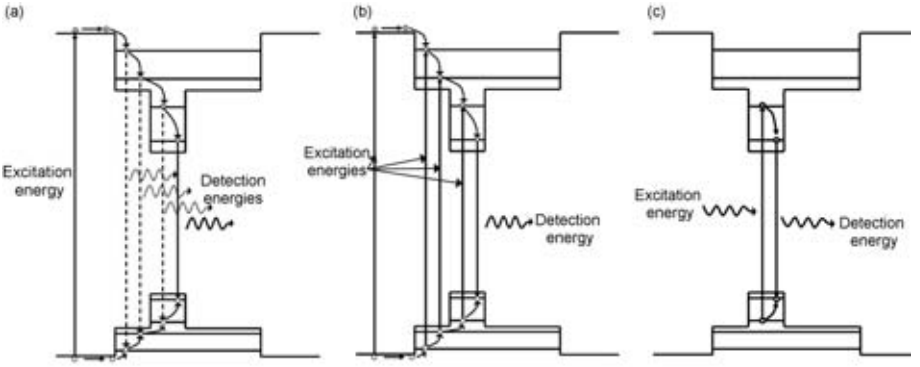

Figure 5.1: Schematic pictures of the principle of (a) photoluminescence (PL) measurements (b) PL excitation measurements (c) Selective PL measurements.

is then kept fixed at the ground state transition energy, while the excitation energy is varied. When the excitation source is resonant with an allowed interband transition, electron-hole-pairs are created, after which electrons and holes relax to the ground state and recombine (Fig. 5.1b)).

5.3 Selective photoluminescence

If the character of a specific excited state interband transition is to be studied in more detail, the excitation energy from the laser can be chosen to be resonant with that specific interband transition energy (Fig. 5.1c), while the ground state emission is detected. The influence of different parameters, such as polarization or intensity of the excitation source, on this specific excited state interband transition can then be obtained.

5.4 Micro photoluminescence

In PL spectroscopy, the luminescence observed is collected from the region of the sample excited by the laser spot. The diameter of the laser spot is of the order of 50-100 μm, when using ordinary lenses. In order to analyze the luminescence from a smaller region, micro-PL can be utilized. By replacing the lens in an ordinary PL setup for an objective lens with large numerical aperture, high spatial resolution can be achieved, typically around 1-2 μm in the NIR region. In order to keep a short distance between the microscope objective and the sample (to enable large numerical apertures), the paths for excitation and collection of the resulting luminescence coincide (backscattering configuration) in the measurement setup at Linköping university (5.2).

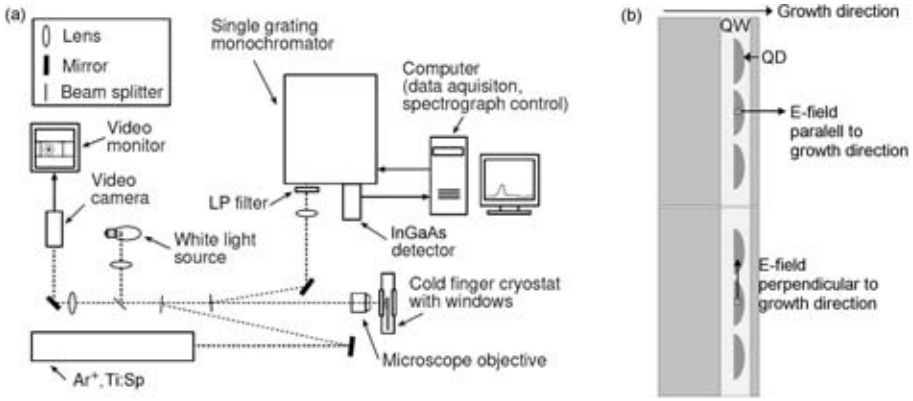

Figure 5.2: (a) Schematic picture of the micro-PL measurement setup. (b) Polarization of E-field with respect to the orientation of the QDs, during polarization dependence measurements, i.e. paralell or perpendicular to the growth direction.

This setup was used to study the polarisation dependence of the luminescence and the absorption in QDs. The polarisation dependence of these processes provides information on the character of the hole states involved in the interband transitions observed in PL and PLE measurements (see section 2.6.1). Linearly polarised light from a titanium:sapphire (Ti:Sp) laser was used as excitation source and the orientation of the polarisation of the incident light is rotated by a $\lambda/2$-plate. The laser spot was focused on a cleaved edge of the sample, enabling orientation of the linear polarisation either parallell or perpendicular to the growth direction (see figure 5.2b). When studying the polarisation dependence of the luminescence, the monochromator will serve as a linear polarizing filter, since it has a favourable orientation of transmission caused by the diffractive gratings. Consequently, the intensity of the luminescence at the entrance of the detector will be dependent on the polarization of the luminescence. By rotation of the luminescence with the $\lambda/2$-plate, the orientation of polarization of the luminescence can be deduced.

5.5 Fourier transform infrared spectroscopy

Fourier transform infrared (FTIR) spectroscopy is based on the principle of a Michelson interferometer (Fig. 5.3 a). In a Michelson interferometer a beam from an external light source is divided into two branches by a semi-transparent beam splitter. The two branches propagate towards two mirrors, one fixed and one moving, where the beams are reflected back towards the beam splitter. The interference between the two beams, when they recombine at the beam splitter, will vary with the optical path difference (OPD) introduced between

the two beams. When the OPD is zero or a multiple of the wavelength of the incident beam, the two beams interfere constructively and the amplitude of the resulting beam is twice the amplitude of a single beam. When the OPD is one half of the wavelength of the incident beam, the intensity of the two beams cancel through destructive interference (Fig. 5.3 b). Consequently, the intensity (I) of the resulting beam leaving the interferometer is modulated with a modulation frequency which dependens on the wavelength (λ) of the incident beam and on the introduced OPD (δ). This dependence is given in equation 5.1, where the variation of the OPD with the scanning speed (v) of the mirror ($\delta = 2vt$) has been inserted.

$$I(\delta) \propto cos(2\pi\frac{\delta}{\lambda}) = cos(4\pi\frac{vt}{\lambda}) \tag{5.1}$$

Simultaneous modulation of a wide wavelength spectrum is enabled in FTIR spectroscopy, since each wavelength gives rise to a unique modulation frequency, $\frac{2v}{\lambda}$. The resulting intensity of the outgoing beam is then the sum of all wavelength components, given by equation 5.2, which can be recognized as the Fourier transform of the spectral distribution. The spectrum, $I(\lambda)$ can consequently be obtained by inverse transformation of the obtained signal.

$$I(\delta) \propto \int_0^\infty I(\lambda)cos(4\pi\frac{vt}{\lambda})d\lambda = \int_{-\infty}^\infty I(\lambda)e^{4\pi\frac{vt}{\lambda}}d\lambda \tag{5.2}$$

This technique can be used for various kinds of measurements, for example photoluminescence (PL), photoluminescence excitation (PLE) and photocurrent (PC) measurements, which are described in sections 5.5.1, 5.5.2 and 5.5.3, respectively.

5.5.1 Fourier transform photoluminescence measurements

With Fourier transform spectroscopy, the advantage of simultaneous detection of the whole wavelength spectrum can be used, for example for photoluminescence measurements. The luminescence from the sample is used as light source in the spectrometer and the modulated luminescence is detected by an external detector (Fig. 5.4).

5.5.2 Fourier transform photoluminescence excitation measurements

When performing photoluminescence excitation measurements with Fourier transform spectroscopy (Fig. 5.5), modulated light from a broad band source is used for simultaneous excitation at all resonant energies. A short-wavelength

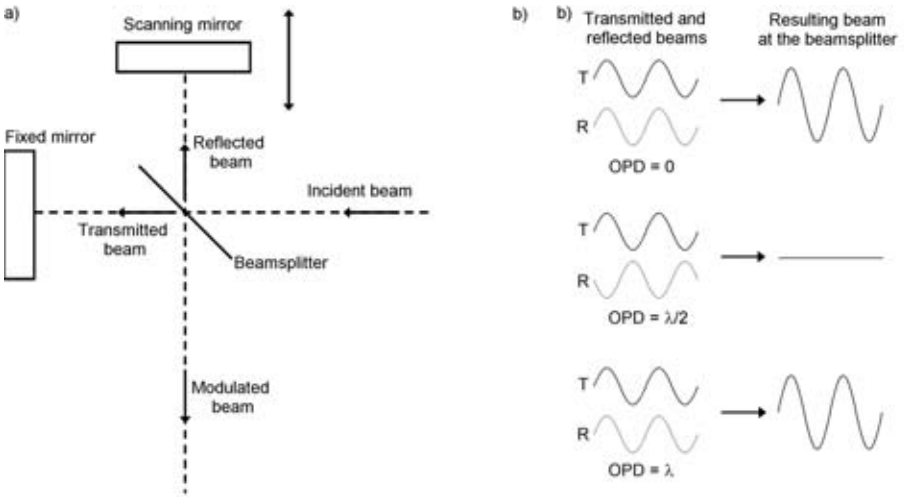

Figure 5.3: a) Schematic picture of the principle of a Michelson interferometer, which creates a modulated beam by introducing an optical path difference (OPD) between the transmitted and the reflected beam b)Variation of the intensity of the resulting beam at the beam splitter with the OPD between the transmitted (T) and reflected (R) beam.

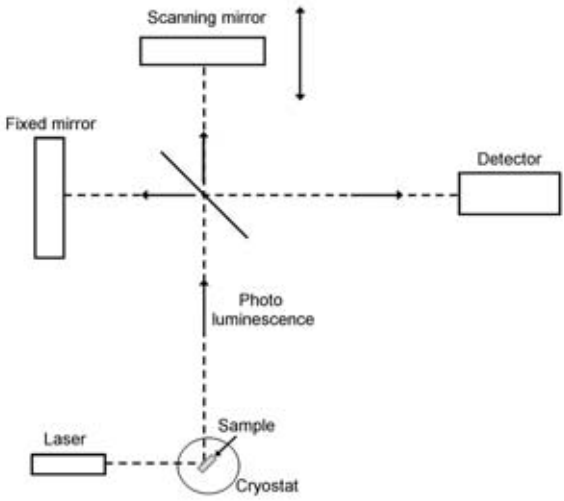

Figure 5.4: Schematic picture of the experimental setup for Fourier transform photoluminescence (FTPL) measurements.

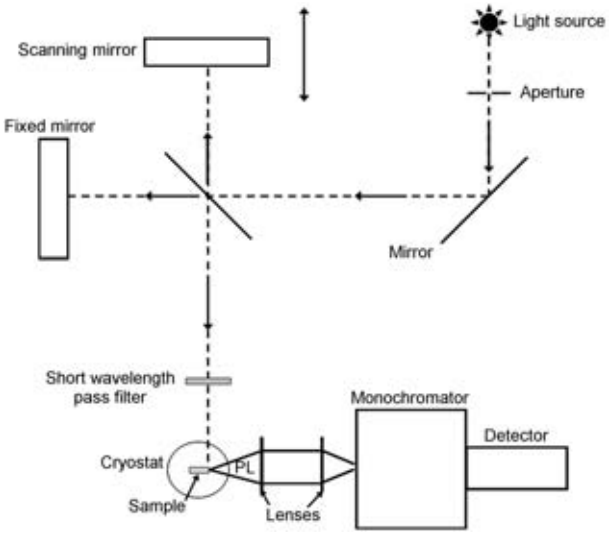

Figure 5.5: Schematic picture of the experimental setup for Fourier transform photoluminescence excitation (FTPLE) measurements.

pass filter is used for the selection of energies higher than the ground state energy. The induced luminescence from the sample is passed through a monochromator, which extracts a certain wavelength region (detection interval) from the luminescence and finally an external detector collects the remaining luminescence. The luminescence corresponding to a certain excitation energy can then be identified through the modulation frequency.

5.5.3 Fourier transform photocurrent measurements

In Fourier transform photocurrent (FTPC) measurements, a broad band source is used to excite carriers and the sample itself is used as a detector (Fig. 5.6). A bias is applied on one contact of the sample and the other contact is used for detection of the generated photocurrent. The photocurrent is amplified by a preamplifier and converted to a voltage before it is analysed in the spectrometer. FTPC measurements can be used to detect intersubband as well as interband transitions (Fig. 5.7). The energy bands of the structure are then tilted by the applied bias, which increases the escape probability from lower lying states in quantum structures. Photocurrent spectra should be normalized with respect to the photon flux to compensate for any variations in the impinging photon flux.

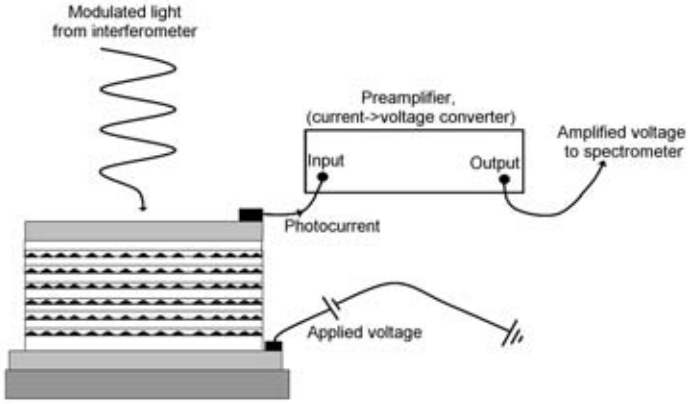

Figure 5.6: Schematic picture of the experimental setup for Fourier transform photocurrent (FTPC) measurements.

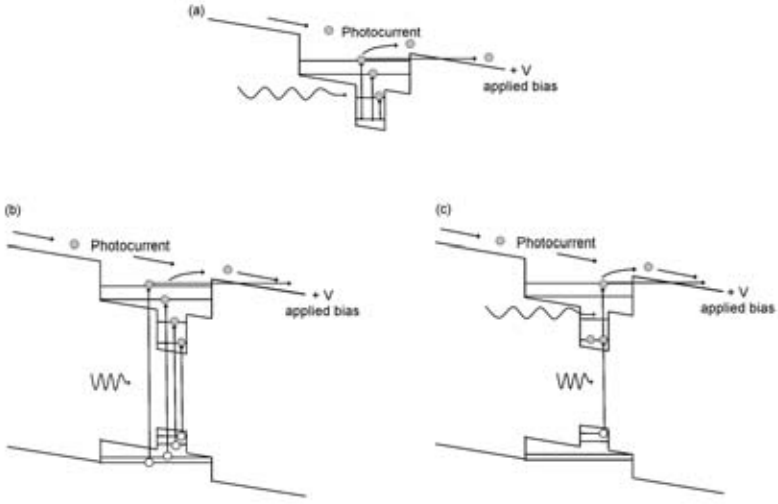

Figure 5.7: Detection principle for (a) intersubband photocurrent measurements (b) interband photocurrent measurements (c) intersubband photocurrent measurements with simultaneous optical pumping.

5.5.4 Photocurrent measurements with optical pumping

Instead of using conventional doping to add extra charge carriers to QDs, optical pumping was used as artificial doping in paper V. A laser with an excitation energy resonant with an interband transition energy of the QD was used, which created electron-hole pairs in the QDs. The number of charge carriers added was regulated by the laser intensity. By using different excitation energies, the electron (and hole) population in different energy levels can be increased. Optical pumping can thus be used to study the contribution to the photocurrent from electrons occupying different energy states in the QD (Fig. 5.7c).

5.6 Dark current measurements

Dark current measurements are performed through measurements of the current (I) for different applied voltages (V). Since the dark current is the current present in the structure without excitation from an external source, the sample is totally shielded during the measurements. The shield should be held at low temperatures in order to avoid thermal emission from the shield itself. The achieved dark current is normally normalised by the area of the device, in order to simplify comparisons with other devices.

5.7 Tunneling capacitance spectroscopy

Tunneling capacitance spectroscopy can be used for determination of the number of bound energy levels, as well as the energy separation between the levels in quantum dots [47, 48, 49, 50]. To accomplish this, a device structure is designed in which the Fermi level can be regulated. When the Fermi level coincides with discrete energy levels in the quantum dots, electrons are induced to tunnel between a highly n-doped contact layer and the quantum dots. The increased charging of the quantum dots is reflected as an increase of the capacitance.

In order to inject electrons into a loaded (with electrons) QD, an additional charging energy is required, which is caused by the Coulomb interaction between the electrons. The additional Coulomb charging energy approximately varies as;

$$E_C(N) = (N - 1/2)\frac{q^2}{C} \tag{5.3}$$

where N is the number of electrons injected into the QDs, q is the electron charge and C is the self-capacitance of the QD (Eq. 2.19) [7]. Consequently, the energies required for the injection of the electrons can be written as: $E_n + E_C(N)$, where E_n is the discrete energy levels of the uncharged QDs

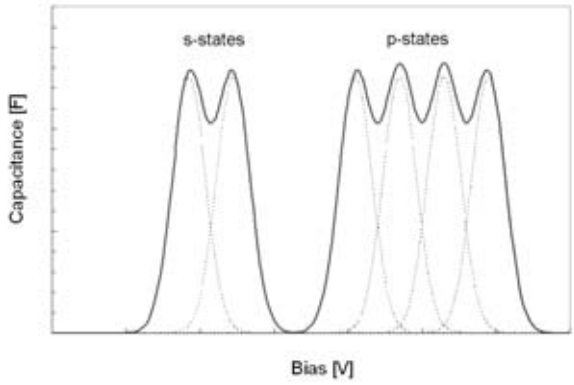

Figure 5.8: Schematic picture of a CV-curve, when charging 6 electrons into the s-, p_x- and p_y-states of a relatively homogeneous ensemble of QDs.

with quantum number n. If the QDs hold s-, p_x- and p_y-states (corresponding to 6 energy states) and the inhomogeneous broadening is small, the injection of electrons to each state can be resolved in a capacitance-voltage (CV) measurement, as shown schematically in figure 5.8. The energy separation between the normally degenerated states (s-states, p-states, etc.) is due to the Coulomb charging energy.

The sample structure used for tunneling capacitance measurements in this study consists of a buried contact layer, a tunneling barrier between the contact layer and the QD layer and finally a capping layer. On the surface of the sample structure, an ohmic contact, which connects to the buried contact layer, and a Schottky contact were fabricated. This configuration results in a region between the contacts, which is depleted from carriers (Fig. 5.9a). In such a configuration, the Fermi level in the structure can be tuned by varying the applied bias (V_A). A positive applied bias lowers the barrier at the Schottky contact ($q\Phi_B$) and consequently the conduction band energy levels approach the Fermi level (Fig. 5.9b,c), while a negative bias results in a higher barrier and an increase of the distance between the Fermi level and the energy levels in the quantum structure. The height of the barrier varies with the applied bias as: $E_{barrier} = q(\Phi_B - V_A)$ (Fig. 5.9). At the position of the QD-layer, this corresponds to an energy separation between the Fermi level and the conduction band edge given by;

$$qV_{QD} = \frac{q(\Phi_b - V_A)}{z_t/z_b} \tag{5.4}$$

i.e. the relation between two congruent triangles.

In order to deduce the number of charge carriers injected into the quantum

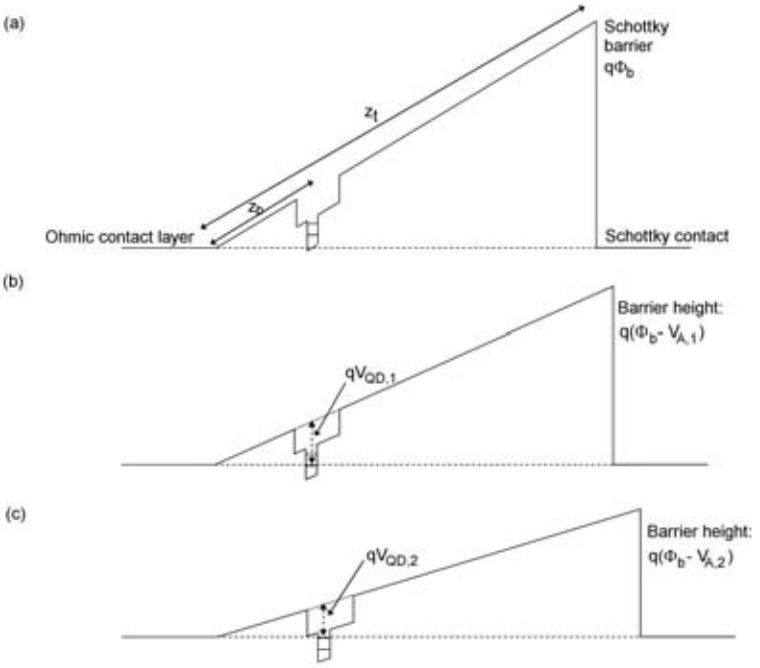

Figure 5.9: Schematic picture of the band alignment between the metal and the semiconductor for different applied biases, V_A: (a) in the unbiased case (b) when applying a positive bias, $V_{A,1}$ (c) when applying a positive bias, $V_{A,2}$.

dots from the CV-measurements, the area under the CV-curve is calculated ($Q = \int C dV_{QD}$) [50]. In figure 5.8, this would result in 6 electrons/QD.

From the bias separation between the peaks, the energy separation can be deduced, using the relation;

$$q(V_{QD,1} - V_{QD,2}) = E_{n,2} + E_C(N_2) - (E_{n,1} + E_C(N_1)) \tag{5.5}$$

where the subscripts 1 and 2 refer to two different applied biases. By inserting equation (5.4) into equation (5.5) a relation between the applied bias and the energy separation is achieved:

$$\frac{q}{z_t/z_b}(V_{A,2} - V_{A,1}) = E_{n,2} - E_{n,1} + (E_C(N_2) - E_C(N_1)) \tag{5.6}$$

$$E_{n,2} - E_{n,1} = \frac{q}{z_t/z_b}(V_{A,2} - V_{A,1}) - (E_C(N_2) - E_C(N_1)) \tag{5.7}$$

5.8 Atomic force microscopy

Atomic force microscopy (AFM) is a method to measure the topography of a surface, by scanning the surface with a sharp tip (Fig. 5.10). The tip is mounted on a cantilever and it interacts with the sample via van der Waals forces. A regulation system is used to keep the force between the tip and the sample constant. Changes in the topography and thereby the force is detected by the deflection of the cantilever. This deflection change is detected by the position of a laser spot, reflected by the cantilever, on a position-sensitive photodetector. In order to compensate for the deflection, a feedback signal is sent to a piezoelectric sample stage, which moves to compensate for the change in force. The movement of the table during scanning of the surface gives information about the topography of the sample.

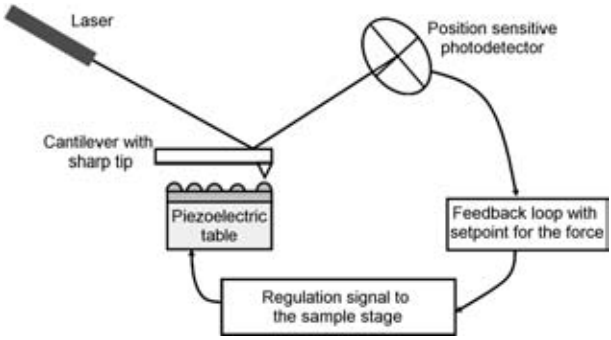

Figure 5.10: Illustration of the measurement setup of a atomic force microscope (AFM).

CHAPTER 6

Summary of the papers

The papers included in this thesis involve growth and characterisation of quantum dot (QD) based material, as well as characterisation of infrared detector components based on QDs. The studies are aiming for an increased understanding of the physical properties of these components.

Paper I

In paper I, a method aiming at finding the right conditions for growth of indium arsenide (InAs) QDs with metal-organic vapour phase epitaxy is presented. The influence of different growth conditions on the size, uniformity and density of QDs is studied. It is shown that the V/III-ratio (the relation between the group V species (arsenide) and the group III species (indium)) in the growth chamber is of major importance for the density of dots. Furthermore, it is found that the uniformity of the dot size distribution is increased at higher growth temperatures, however, at the expense of lower dot density.

Paper II

The growth techniques described in paper I have been used to fabricate infrared detector structures based on InAs QDs embedded in indium gallium arsenide / gallium arsenide quantum wells (QWs). Paper II investigates the origin of the photocurrent (PC) in lateral DWELL IPs, utilising optical and optoelectronical measurements. Optical measurements of the interband transitions, using Fourier transform photoluminescence (FTPL) and FTPL exci-

tation, serve to derive an energy level scheme of the DWELL structure. The obtained level scheme is compared with the results of the PC measurements in order to deduce the intersubband transitions responsible for the observed PC. It is concluded that the intersubband transitions from the QD ground states to a QW excited state give the strongest contribution to the PC. This fact is shown to be valid also for vertical DWELL IPs, which have been studied in paper III with the same method as in paper II.

Paper III

In Paper III, the escape mechanisms in a vertical DWELL IP are studied by means of temperature and bias dependence of intersubband photocurrent measurements, as well as dark current measurements. A strong bias dependence of the intersubband photocurrent is observed, which is attributed to the increasing tunneling probability with increasing bias, from the energetically deep energy levels in the QW. Thermal assistance also plays an important role in the escape process, causing a strong temperature dependence of the intersubband photocurrent. Using interband photocurrent measurements, substantial escape of electrons from lower lying states in the DWELL structure at large biases is revealed, which could explain the strong temperature and bias dependence of the dark current in DWELL IPs.

Paper IV

In paper IV, one of the advantages of the dots-in-a-well detector concept is demonstrated: the possibility to achieve dual colour detection within the same pixel by varying the applied bias. Bias-mediated tuning of the detection wavelength is demonstrated for two different detector structures: an asymmetrical quantum dots-in-a-well structure and a dots-on-a-well structure. Tuning within the long wavelength infrared region, from 8.4 to 10.3 μm, is achieved for the dots-in-a-well structure. The tuning is enabled due to the asymmetrical positioning of the InAs QD layer in the $In_{0.15}Ga_{0.85}As$/GaAs QW, which induces a quantum-confined Stark shift in the structure. When the QD layer instead is positioned on top of a thin $In_{0.15}Ga_{0.85}As$/GaAs QW, tuning from the medium wavelength infrared region to the long wavelength infrared is enabled, i.e. from 5.4 to 8 μm. In this structure, the detector utilizes two different strongly bias-dependent photocurrent peaks, which alternately dominate the photocurrent spectra.

Paper V

In paper V, the achievable responsivity of the dots-in-a-well detector is investigated by using optical pumping as artificial doping in the QDs. It is shown that the responsivity could be increased to at least 250 mA/W, if a sufficient

number of carriers is supplied. Furthermore, optical pumping is used to identify the origin of two photocurrent peaks observed at 120 and 148 meV. By selectively increasing the electron population in the ground states and the excited states of the QDs, respectively, the influence from these two states on the photocurrent peaks are observed. It is shown that the 120 and 148 meV peaks originate from intersubband transitions with the initial states as the excited states and the ground states of the QDs, respectively.

Paper VI

Finally, in paper VI a more thorough investigation of the energy level structure in a DWELL IP is studied with a combination of several different experimental techniques. From interband measurements, such as photoluminescene (PL) and PL excitation, the interband transitions occuring in a DWELL are achieved, from which approximate energy level schemes of the conduction and valence band energy structures are deduced. By studying the polarization dependence of the quantum dot interband transitions, it is revealed that the QDs hold two electron and two heavy hole energy levels. An electron energy level separation of 50 meV is deduced from tunneling capacitance measurements. Using the knowledge obtained in paper III, that the final state of the dominant intersubband transition is a bound state in the QW, the QD-QW energy level separation is obtained from photocurrent measurements. When summarizing these results, an almost complete energy level structure of the DWELL infrared photodetector is obtained.

Bibliography

[1] L. Esaki and R. Tsu, IBM Journal of Research and Development, **14**, 61 (1970).

[2] V. Ryzhii, Semicond. Sci. Technol. **11**, 759 (1996).

[3] J.R. Chelikowsky, M.L. Cohen, Phys. Rev B, **14**, 556 (1976).

[4] P. Harrison, *Quantum Wells, Wires and Dots, 2nd edition* (John Wiley & Sons 2005)

[5] I. Vurgaftman, J. R. Meyer, L.R.Ram-Mohan, J. of Appl. Phys. **89**, 5815 (2001).

[6] A.J. Williamson, L.W. Wang, A. Zunger, Phys. Rev. B, **62**, 12963 (2000).

[7] H. Drexler, D. Leonard, W. Hansen, J. P. Kotthaus, P. M. Petroff, Phys. Rev. Lett. **73**, 2252 (1994).

[8] G. Bastard, E. E. Mendez, L. L. Chang, L. Esaki, Phys. Rev. B, **28**, 3241 (1983).

[9] H. C. Liu *Intersubband transitions in Quantum wells; Physics and Device applications I, Semiconductors and Semimetals*, Vol 62, ed R. K. Williardson and E. R. Weber (San Diego:Academic).

[10] P. F. Yuh, K. L. Wang, IEEE J. of Quantum Electronics, **25**, 1671 (1989).

[11] Y. J. Mii, R. P. G. Karunasiri, K. L. Wang, M. Chen, P. F. Yuh, Appl. Phys. Lett. **56**, 1986 (1990).

[12] P.A. Martin, B. G. Streetman, K. Hess, J. of Appl. Phys. **52**, 7409 (1981).

[13] G. Vincent, A. Chantre, D. Bois, J. of Appl. Phys. **50**, 5484 (1979).

[14] K.W. Böer, *Survey of semiconductor physics* (John Wiley & Sons 2002).

[15] Ashcroft/Mermin *Solid state physics* (Thomson Learning, Inc. 1976).

[16] C.M. Wolfe, N. Holonyak, Jr, G.E. Stillman *Physical properties of semiconductors* (Prentice-Hall, Inc. 1989).

[17] J.H. Davies *The physics of low-dimensional semiconductors* (Cambridge University Press 1998).

[18] M. Schlessinger, *Infrared Technology Fundamentals* (Marcel Dekker, inc 1995).

[19] A. Rogalski, Infrared Phys. & Tech, **43**, 187 (2002).

[20] B. Hirschauer, J.Y. Andersson, J. Alverbro, U. Halldin, H. Malm, H.H. Martijn, C. Nordahl, U. Norden, Proc. of SPIE, **4820**, 107 (2003).

[21] J.Y. Andersson, L. Lundqvist, J. Appl. Phys. **71**, 3600 (1992).

[22] E. Merzbacher, *Quantum Mechanics*, (John Wiley & Sons 1998).

[23] M.A. Herman, W. Richter, H. Sitter, *Epitaxy, Physical Principles and Technical Implementation* (Springer, 2004).

[24] W. Seifert, N. Carlsson, J. Johansson, M.E. Pistol, L. Samuelsson, Journal of Crystal Growth, **170** 39 (1997).

[25] A.R. Woll, P. Rugheimer, M.G. Lagally, International Journal of High Speed Electronics and Systems, **12**, 45 (2002).

[26] R.B. Johnson, Proc. of SPIE, **915**, 102 (1988).

[27] P.W. Kruse *The photon detection process* in *Optical and infrared detectors*, Ed. R. J. Keyes (Springer-Verlag, 1977).

[28] E.-T. Kim, A. Madhukar, Z. Ye, J.C. Campbell, Appl. Phys. Lett. **84**, 3277 (2004).

[29] S. Krishna, J. Phys. D, Appl. Phys. **38**, 2142 (2005).

[30] S. Raghavan, D. Forman, P. Hill, N.R. Weisse-Bernstein, G. von Winckel, P. Rotella, S. Krishna, S.W. Kennerly, J.W. Little, J. Appl. Phys. **96**, 1036 (2004).

[31] E.T. Kim, Z.Chen, A. Madhukar, Appl. Phys. Lett. **81**, 3473 (2002).

[32] S. Krishna, D. Forman, S. Annamalai, P. Dowd, P. Varangis, T. Tumolillo, A. Gray, J. Zilko, K. Sun, M. Liu, J. Campbell, D. Carothers, Phys. Stat. Sol (c), **3**, 439 (2006).

[33] P. Aivaliotis, N. Vukmirovic, E. A. Zibik, J. W. Cockburn, D. Indjin, P. Harrison, C. Groves, J. P. R. David, M. Hopkinson, L. R. Wilson, J. Phys. D.: Appl. Phys. **40**, 5537 (2007).

[34] S. Krishna, S. Raghavan, G. von Winckel, A. Stintz, G. Ariyawansa, S. G. Matsik, A. G. U. Perera, Appl. Phys. Lett. **83**, 2745 (2003).

[35] L. Ouattara, A. Mikkelsen, E. Lundgren, L. Höglund, C. Asplund, J. Y. Andersson, J. Appl. Phys. **100**, 044320 (2006).

[36] H.C. Liu, *The Basic Physics of Photoconductive Quantum Well Infrared Photodetectors* in *Long Wavelength Infrared Detectors*, ed. M.Razeghi (Langhorne, PA: Gordon and Breach 1995).

[37] T. Müller, F. F. Schrey, G. Strasser, K. Unterrainer, Appl. Phys. Lett. **83**, 3572 (2003).

[38] B. F. Levine, J. Appl. Phys. **74**, R1 (1993).

[39] B. Kochman, A.D. Stiff Roberts, S. Chakrabati, J.D. Phillips, S. Krishna, J. Singh, P. Bhattacharya, IEEE Journal of Quantum Electronics, **39**, 459 (2003).

[40] P. Martyniuk, A. Rogalski, Proc. of SPIE, **6940**, 694004-1 (2008).

[41] M.C. Tatham, J.F. Ryan, C.T. Foxon, Phys. Rev. Lett. **63** 1637 (1989).

[42] J. Urayama, T.B. Norris, J. Singh, P. Bhattacharya et al Phys. Rev. Lett. **86**, 4930 (2001).

[43] S. D. Gunapala, S. V. Bandara, C. J. Hill, D. Z. Ting, J. K. Liu, S. B. Rafol, E. R. Blazejewski, J. M. Mumolo, S. A. Keo, S. Krishna, Y. C. Chang, C. A. Shott, Proc. of SPIE, **6206**, 62060J-2 (2006).

[44] B.F. Levine, C. G. Bethea, G. Hasnain, V. O. Shen, E. Pelve, R. R. Abbott, S. J. Hsieh, Appl. Phys. Lett. **56**, 851 (1990).

[45] M. A. Kinch, J. of Electronic Materials, **29**, 809 (2000).

[46] V. Ryzhii, V. Pipa, I. Khmyrova, V. Mittin, M. Willander, Jpn J. Appl. Phys. **39**, 1283 (2000).

[47] M. Fricke, A. Lorke, J. P. Kotthaus, G. Medeiros-Ribeiro, P. M. Petroff, Europhys. Lett. **36**, 197 (1996).

[48] B. T. Miller, W. Hansen, S. Manus, R. J. Luyken, A. Lorke, J. P. Kotthaus, Phys. Rev. B, **56**, 6764 (1997).

[49] H. Pettersson, R. J. Warburton, J. P. Kotthaus, N. Carlsson, W. Seifert, M. -E. Pistol, L. Samuelsson, Phys. Rev. B, **60**, 11290 (1999).

[50] R.C. Ashoori, H. L. Stormer, J. S. Weiner, L. N. Pfeiffer, S. J. Pearton, K. W. Baldwin, K. W. West, Phys. Rev. Lett. **68**, 3088 (1992).